Supporting Information

for

Aviation contrail climate effects in the North Atlantic Region from 2016-2021

Roger Teoh[1], Ulrich Schumann[2], Edward Gryspeerdt[3], Marc Shapiro[4], Jarlath Molloy[5], George Koudis[5], Christiane Voigt[2,6] and Marc E.J. Stettler[1]*

[1] Centre for Transport Studies, Department of Civil and Environmental Engineering, Imperial College London, London, SW7 2AZ, United Kingdom

[2] Institute of Atmospheric Physics, Deutsches Zentrum für Luft- und Raumfahrt, 82234 Oberpfaffenhofen, Germany

[3] Grantham Institute – Climate Change and Environment, Imperial College London, London, SW7 2AZ, United Kingdom

[4] Orca Sciences, 4110 Carillon Point, Kirkland, WA 98033, United States

[5] NATS, 4000 Parkway, Whiteley, Fareham, Hampshire, PO15 7FL, United Kingdom

[6] Institute of Atmospheric Physics, University Mainz, 55099 Mainz, Germany

* Corresponding author: m.stettler@imperial.ac.uk

Supporting Information Details:

- Number of pages: 39
- Number of figures: 24
- Number of tables: 7

Contents

S1 Air Traffic Dataset 3

S2 nvPM Number Emissions Index 7

S2.1 Background Information 7

S2.2 Methodology 10

S2.3 Example & Comparison 14

S3 Correction to ERA5 humidity fields 16

S4 Conditions for forming strongly warming/cooling contrails 25

S5 Uncertainty analysis 29

S6 Sensitivity analysis 33

References 37

S1 Air Traffic Dataset

The air traffic dataset used in this study is provided by the UK air navigation service provider (NATS) for the period between 1-January-2016 and 31-March-2021. There are 2,106,317 recorded civil flights in the dataset and the following information is provided for each flight:

- call sign,
- operator,
- ICAO airport code for the origin and destination airports,
- ICAO aircraft type designator,
- up to 10 waypoints containing the 4D positional data (longitude, latitude, altitude, and time) are recorded when the flight passes through a series of fixed waypoints along the route, and
- any air traffic commands when the flight executes a step climb/descent in between the recorded waypoints.

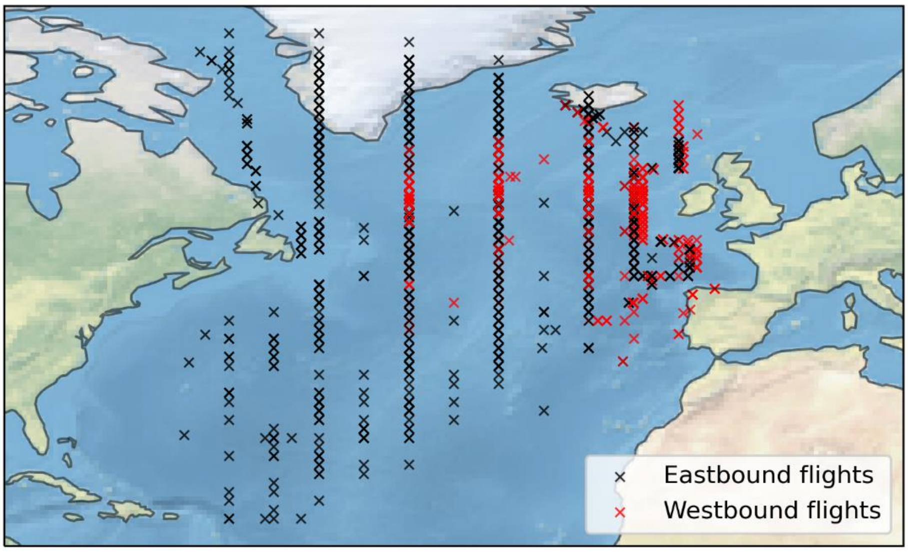

Figure S1: Waypoints that are provided by the NATS air traffic dataset for 1-January-2019. Basemap plotted using Cartopy 0.20.2 (C) Natural Earth; license: public domain.

Figure S1 shows an example of the waypoints that are provided by the NATS dataset for 1-January-2019. As noted in the main text (Section 2.1) and demonstrated in Fig. S1, waypoints for eastbound flights are available before the flights enters the Shanwick OACC (between 10°W to 70°W); while waypoints for westbound flights are not available outside Shanwick (10°W to 40°W). We perform a great circle interpolation at a constant flight level between: (i) the recorded waypoints; (ii) the origin airport and first recorded waypoint; and (iii) the final recorded waypoint and the destination airport to obtain a full trajectory coverage in the Shanwick and Gander OACC (Fig. S2 and S3) with a uniform temporal resolution of 60 s (average segment length of 15 km). Any waypoints outside Shanwick and Gander are then removed, and the processed dataset, therefore, approximates the air traffic activity in the North Atlantic flight corridor (Fig. S4). We assume the spatial bounding box of the Shanwick and Gander OACC to be (50°W, 40°N, 10°W, 75°N) minus the air traffic activity in the Shannon OACC (15°W, 51°N, 10°W, 54.5°N), and the total surface area in this region is equal to 9.026 $\times 10^{12}$ m^2.

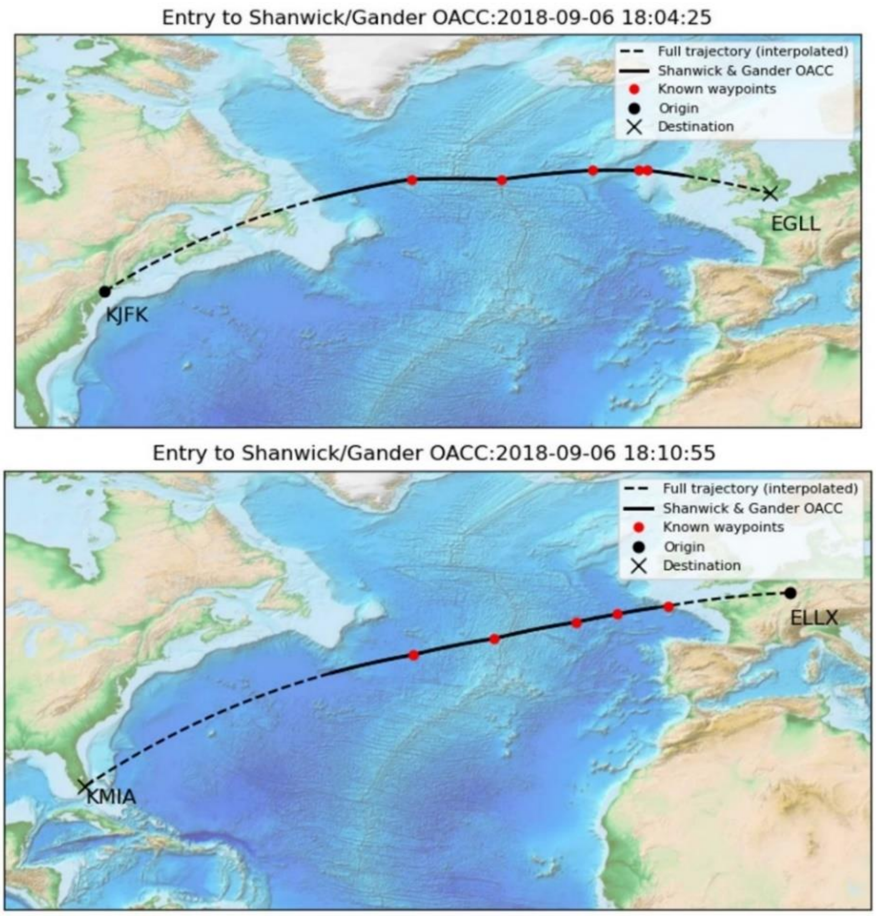

Figure S2: Examples of the flight trajectories in the processed NATS dataset. The data points in red are waypoints that are provided by the original NATS dataset, the solid black lines connecting the recorded waypoints are interpolated by assuming a great circle distance. Basemap plotted using Cartopy 0.20.2 (C) Natural Earth; license: public domain.

Figure S3: Boundaries of the Shanwick and Gander OACC, which covers the air traffic activity in the North Atlantic flight corridor. (Source: NATS (2014)**)**

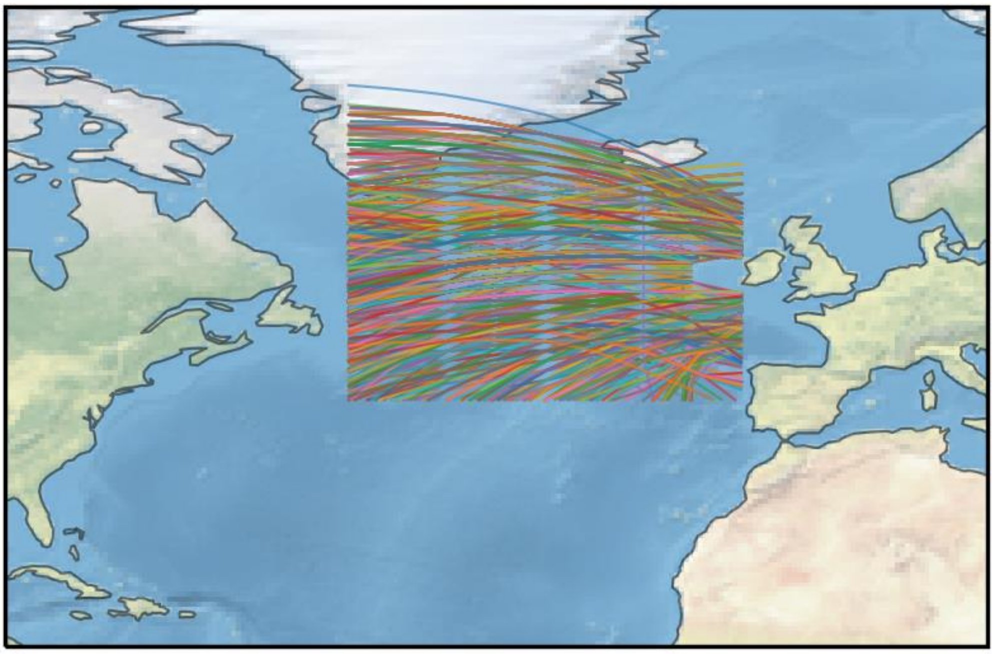

Figure S4: Example of the flight trajectories from the processed NATS dataset for 1-January-2019. Each line represents the trajectory of a single flight. Basemap plotted using Cartopy 0.20.2 (C) Natural Earth; license: public domain.

The air traffic density in this region is calculated by dividing the total flight distance per hour with the airspace area (9.026×10^{12} m^2). Figure S5a shows that the air traffic density in the North Atlantic region for 2019 ranges from 0.002 to 0.034 km^{-1} h^{-1}. This range is smaller than the values reported by Schumann & Graf (2013), between 0.01 and 0.05 km^{-1} h^{-1}, because we considered a larger spatial domain (refer to the spatial bounding boxes in Fig. S5b). For comparison, the air traffic density in Europe and North America are estimated to be above 0.06 km^{-1} h^{-1} (Schumann and Graf, 2013). Figure S6 provides a breakdown of the fleet composition by aircraft type and its evolution over time.

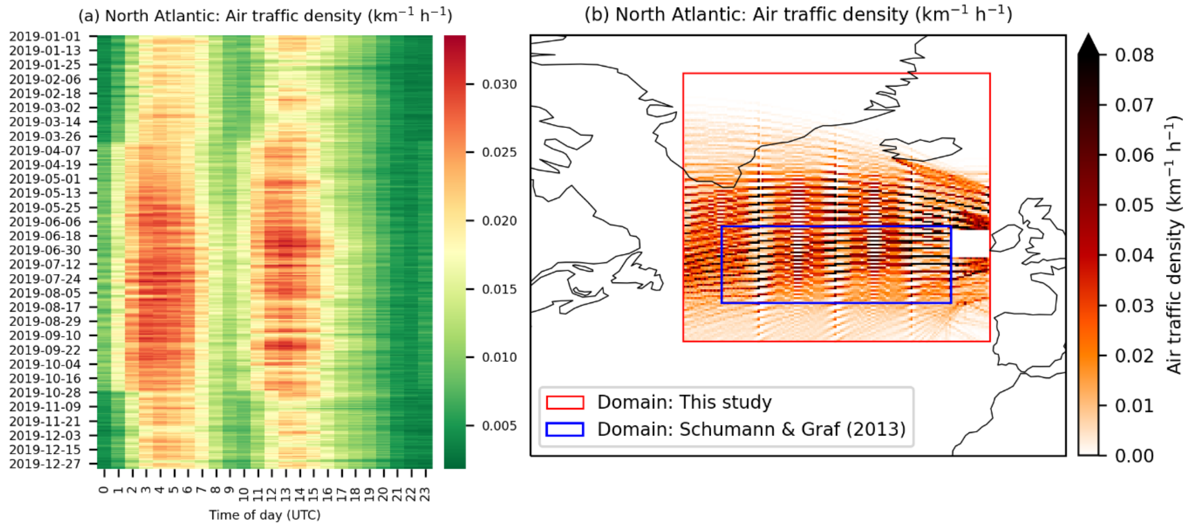

Figure S5: The air traffic density in the North Atlantic region by distance travelled that is averaged (a) for each hour; and (b) across the spatial domain for 2019. Basemap plotted using Cartopy 0.20.2 (C) Natural Earth; license: public domain.

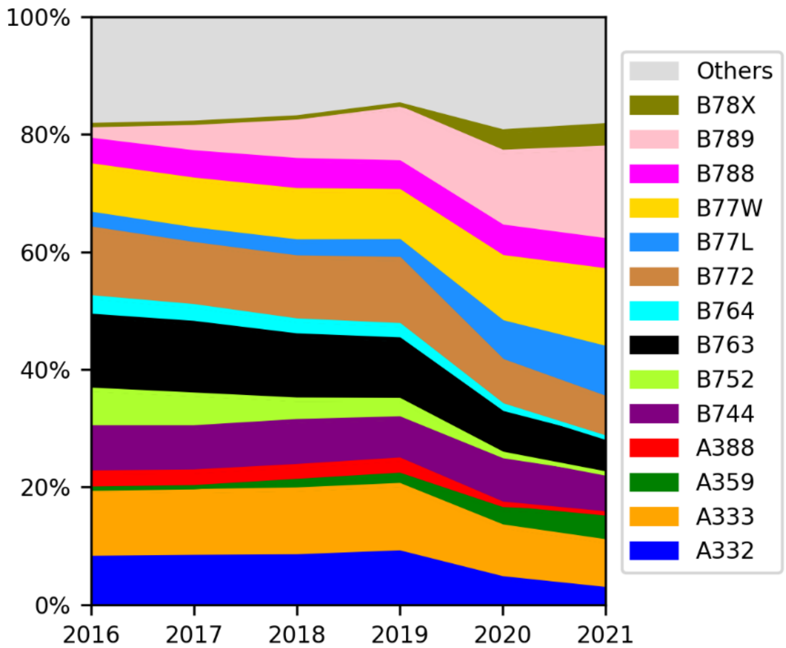

Figure S6: Fleet composition by aircraft type for all flights that traversed the Shanwick and Gander OACC between January-2016 to March-2021

S2 nvPM Number Emissions Index

S2.1 Background Information

A new dataset containing measurements of non-volatile particulate matter (nvPM) emissions from turbofan engines has been added to the International Civil Aviation Organization (ICAO)

Aircraft Emissions Databank (EDB) in December 2020 (ICAO, 2021). This dataset is publicly available and contains 194 distinct turbofan engines, including those that are currently in production and new aircraft engine types with a rated thrust above 26.7 kN. For each engine, the measured nvPM number (EI_n in kg^{-1}) and mass emissions index (EI_m in g kg^{-1}) is reported at the four ICAO certification test points (7%, 30%, 85% and 100% of the maximum rated engine thrust) that represent the engine power settings typically used in a landing and take-off (LTO) cycle. These nvPM measurements have been corrected for dilution, thermophoretic and particle line losses (EASA, 2020).

We used the Base of Aircraft Data (BADA) Family 3 and 4 databases to match a given aircraft type to an engine (Eurocontrol, 2016, 2014). Table S1 compiles the 47 aircraft-engine pairs that have been successfully identified. An exploratory data analysis of the dataset showed that the combustor type of different turbofan engines can lead to large differences in the emissions profile for the nvPM EI_n and EI_m (Fig. S7): the nvPM EI_n from twin annular premixing swirler (TAPS) engines that power the Boeing 737 MAX, Boeing 747-800 and Boeing 787-10 Dreamliner decreases from 10^{14} kg^{-1} to 10^{11} kg^{-1} with increasing engine power (Fig. S7i and S7j), while the EI_n for Floatwall combustors that are equipped by the Airbus A320ceo has a smaller range but stays high at around 3 to 7 $\times 10^{15}$ kg^{-1} (Fig. S7b). These results highlight the need to develop a new approach to estimate the nvPM emissions that can capture the distinct emissions profile for different combustor types.

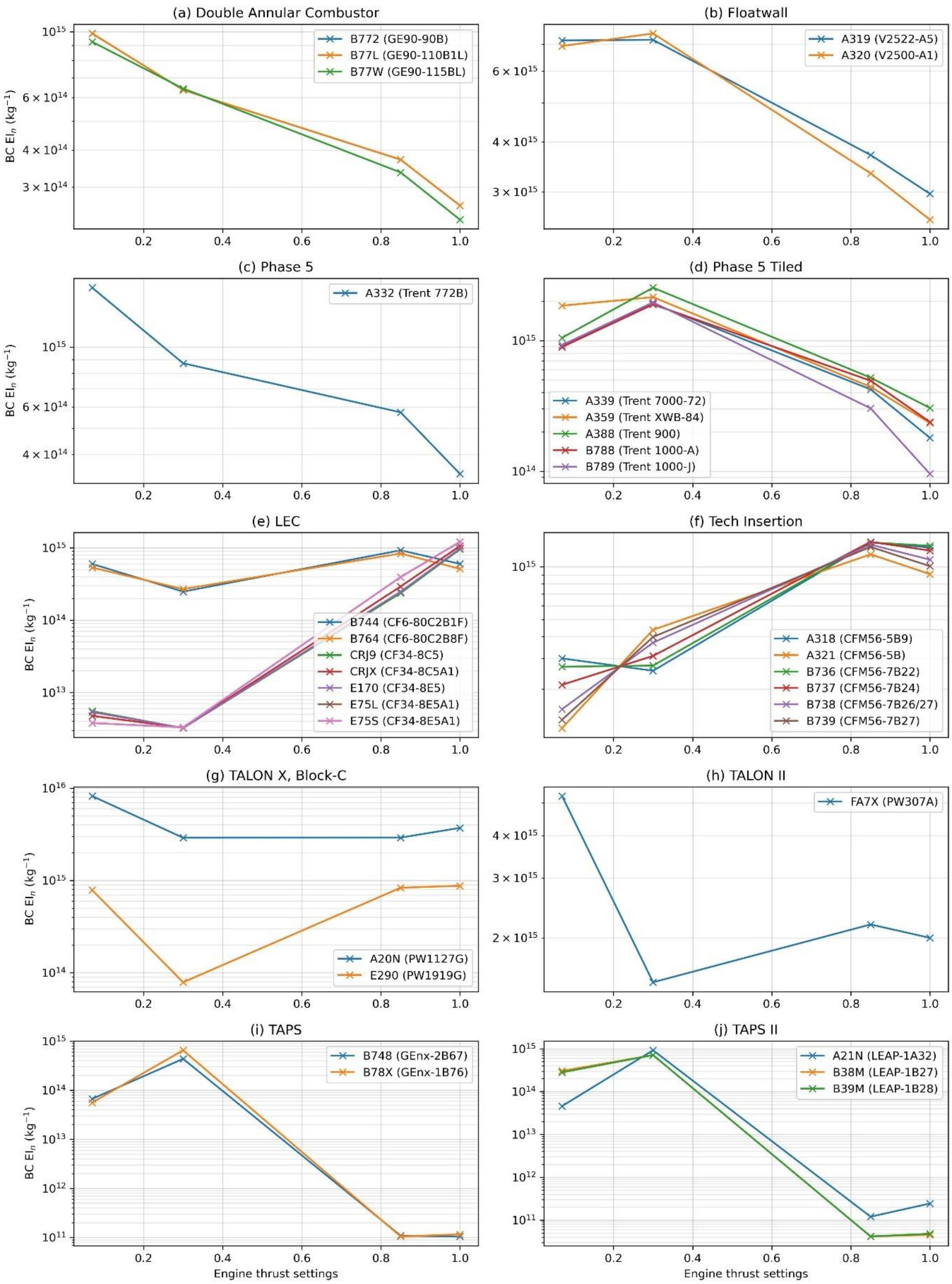

Figure S7: ICAO EDB measurements of the nvPM EI$_n$ (corrected for system loss) at the four ICAO certification test points (7%, 30%, 85% and 100% of the maximum rated engine thrust) by combustor type and aircraft-engine pairs.

S2.2 Methodology

In this study, we used measurements from the ICAO EDB to develop an approach to estimate the nvPM EI_n at cruise conditions (ICAO, 2021). This approach is based on linear interpolation of the nvPM measurements relative to the engine power, which is comparable to the Fuel Flow Method 2 (FFM2) methodology that was developed to estimate the nitrogen oxide emission indices (EI_{NOx}) at cruise conditions (DuBois and Paynter, 2006).

Table S1: Compilation of the aircraft-engine assignment list that is used to obtain the engine-specific NO_x emissions and nvPM EI_n from the ICAO EDB.

Aircraft Type	ICAO Code	Engine Identification	Manufacturer	Combustor Description
Airbus A320neo	A20N	PW1127G	Pratt & Whitney	TALON X, Block-C
Airbus A321neo	A21N	LEAP-1A32	CFM International	TAPS II
Airbus A318	A318	CFM56-5B9	CFM International	Tech Insertion
Airbus A319	A319	V2522-A5	International Aero Engines	Floatwall
Airbus A320	A320	V2527-A5	International Aero Engines	Floatwall
Airbus A321	A321	CFM56-5B	CFM International	Tech Insertion
Airbus A330-200	A332	Trent 772B	Rolls-Royce plc	Phase5
Airbus A330-900	A339	Trent 7000-72	Rolls-Royce plc	Phase5 Tiled
Airbus A350-900	A359	Trent XWB-84	Rolls-Royce plc	Phase5 Tiled
Airbus A350-1000	A35K	Trent XWB-97	Rolls-Royce plc	Phase5 Tiled (Improved)
Airbus A380-800	A388	Trent 900	Rolls-Royce plc	Phase5 Tiled
Boeing 737 MAX 8	B38M	LEAP-1B27	CFM International	TAPS II
Boeing 737 MAX 9	B39M	LEAP-1B28	CFM International	TAPS II
Boeing 737-600	B736	CFM56-7B22	CFM International	Tech Insertion
Boeing 737-700	B737	CFM56-7B24	CFM International	Tech Insertion
Boeing 737-800	B738	CFM56-7B26/27	CFM International	Tech Insertion
Boeing 737-900	B739	CFM56-7B27	CFM International	Tech Insertion
Boeing 747-400	B744	CF6-80C2B1F	General Electric Company	LEC
Boeing 747-8F	B748	GEnx-2B67	General Electric Company	TAPS
Boeing 767-400ER	B764	CF6-80C2B8F	General Electric Company	LEC
Boeing 777-200	B772	GE90-90B	General Electric Company	DAC
Boeing 777-200 Freighter	B77L	GE90-110B1L	General Electric Company	DAC
Boeing 777-300ER	B77W	GE90-115BL	General Electric Company	DAC
Boeing 787-8	B788	Trent 1000-A	Rolls-Royce plc	Phase5 Tiled
Boeing 787-9	B789	Trent 1000-J	Rolls-Royce plc	Phase5 Tiled
Boeing 787-10	B78X	GEnx-1B76	General Electric Company	TAPS

Bombardier Challenger 300	CL30	AS907-1-1A	Honeywell	SABER-1
Canadair Challenger	CL60	CF34-3B	General Electric Company	SAC
Canadair Regional Jet 200	CRJ2	CF34-3B1	General Electric Company	SAC
Canadair Regional Jet 900	CRJ9	CF34-8C5	General Electric Company	LEC
Canadair Regional Jet 1000	CRJX	CF34-8C5A1	General Electric Company	LEC
Embraer RJ135	E135	AE 3007A1/3	Rolls-Royce Corporation	Type 3 (reduced emissions)
Embraer RJ145	E145	AE 3007A1	Rolls-Royce Corporation	Type 3 (reduced emissions)
Embraer 170	E170	CF34-8E5	General Electric Company	LEC
Embraer E190-E2	E290	PW1919G	Pratt & Whitney	TALON X, Block-C
Embraer Legacy 600	E35L	AE 3007A1E	Rolls-Royce Corporation	Type 3 (reduced emissions)
Embraer ERJ-145XR	E45X	AE 3007A1E	Rolls-Royce Corporation	Type 3 (reduced emissions)
Embraer Legacy 450	E545	AS907-3-1E	Honeywell	SABER-1
Embraer Legacy 500	E550	AS907-3-1E	Honeywell	SABER-1
Embraer 175 (long wing)	E75L	CF34-8E5A1	General Electric Company	LEC
Embraer 175 (short wing)	E75S	CF34-8E5A1	General Electric Company	LEC
Dassault Falcon 7X	FA7X	PW307A	Pratt & Whitney Canada	TALON II
Bombardier Global 5000	GL5T	BR700-710A2-20	Rolls-Royce Deutschland	
Bombardier Global Express	GLEX	BR700-710A2-20	Rolls-Royce Deutschland	
Gulfstream V	GLF5	BR700-710C4-11	Rolls-Royce Deutschland	Annular
Hawker 4000	HA4T	PW308A	Pratt & Whitney Canada	Annular
Sukhoi Superjet 100-95	SU95	SaM146-1S17	PowerJet S.A.	

For each engine, the engine thrust settings ($\frac{F}{F_{00,\mathrm{max}}}$) at the four ICAO certification test points are first estimated by dividing the fuel mass flow rate ($\dot{m}_{\mathrm{f}}$ in kg s^{-1}) by the maximum fuel mass flow rate ($\dot{m}_{\mathrm{f,max}}$), both of which are provided in the ICAO EDB,

$$\frac{F}{F_{00,\mathrm{max}}} = \frac{\dot{m}_{\mathrm{f}}}{\dot{m}_{\mathrm{f,max}}}, \tag{S1}$$

where $\dot{m}_{\mathrm{f,max}}$ is assumed to be the fuel mass flow rate at take-off conditions. Once $\frac{F}{F_{00,\mathrm{max}}}$ is available, we calculate the thermodynamic quantities at different sections of the turbofan engine to estimate the ratio of turbine inlet to compressor inlet temperatures (T_4/T_2), a non-dimensional measure of engine power that account for differences in operating conditions at ground and cruise conditions (Cumpsty and Heyes, 2015). The use of T_4/T_2 circumvents the need for a cruise scaling equation such as the Döpelheuer & Lecht method (1998), as will be shown in §S2.3.

First, the compressor inlet pressure (P_2) and temperature (T_2) are calculated,

$$P_2[\mathrm{Pa}] = P_{\mathrm{amb}}(1 + \frac{\gamma-1}{2} M_a{}^2)^{\frac{\gamma}{\gamma-1}}, \tag{S2}$$

$$T_2[\mathrm{K}] = T_{\mathrm{amb}}\left(1 + \frac{\gamma-1}{2} M_a{}^2\right), \tag{S3}$$

where $\gamma = 1.4$ is the ratio of specific heats, P_{amb} is the ambient pressure, T_{amb} is the ambient temperature and Ma is the aircraft Mach number. For conditions on the ground, we assume that P_{amb} = 101325 Pa, Ma = 0, and T_{amb} values are provided in the ICAO EDB.

Next, we estimate the combustor inlet pressure (P_3) and temperature (T_3),

$$P_3[\mathrm{Pa}] = P_2(\pi_{00} - 1)\left(\frac{F}{F_{00,\mathrm{max}}}\right) + P_2, \tag{S4}$$

$$T_3[\mathrm{K}] = T_2(\frac{P_3}{P_2})^{\frac{\gamma-1}{\gamma n_p}}, \tag{S5}$$

where π_{00} is the engine pressure ratio provided in the ICAO EDB and $n_p = 0.9$ is the compressor efficiency. Finally, the turbine inlet temperature (T_4) is calculated,

$$T_4[\mathrm{K}] = \frac{\mathrm{AFR}\ c_{\mathrm{p,a}}\ T_3 + \mathrm{LCV}}{c_{\mathrm{p,e}}\ (1+\mathrm{AFR})}, \tag{S6}$$

where $$\mathrm{AFR}_{\mathrm{ground}} = \left(0.0121\left(\frac{F}{F_{00,\mathrm{max}}}\right) + 0.008\right)^{-1}, \quad \text{and} \tag{S7}$$

$$\mathrm{AFR}_{\mathrm{cruise}} = \mathrm{AFR}_{\mathrm{ground}}(\frac{T_2}{T_{\mathrm{msl}}}). \tag{S8}$$

AFR is the air-to-fuel ratio, $c_{p,a}$ = 1005 J kg^{-1} K^{-1} and $c_{p,e}$ =1250 J kg^{-1} K^{-1} are the heat capacity at a constant pressure of air and for combustion products, LCV = 43.2 MJ kg^{-1} is the lower calorific value of kerosene, and T_{msl} = 288.15 K is the temperature at mean sea level. We note that these thermodynamic equations (P_2, T_2, P_3, T_3 and T_4) are widely used in the literature to model the thermodynamic performance of jet engines (Cumpsty and Heyes, 2015; Agarwal et al., 2019; Stettler et al., 2013), and have also been validated with data provided by flight data recorders (Stettler et al., 2013; Stettler, 2013). Eq. (S7) that is used to estimate the AFR_{ground} was formulated using data from five different engine types (Stettler et al., 2013), while the AFR scaling from ground to cruise, Eq. (S8), is based on a standard non-dimensional analysis from DuBois & Paynter (2006).

Once the T_4/T_2 is calculated at the four ICAO certification test points, we formulated a relationship between the nvPM EI_n and T_4/T_2 by assuming a linear fit between each pair of points. The estimated T_4/T_2 at cruise conditions are then used to interpolate the nvPM EI_n. While more detailed measurements have shown that the nvPM emissions profile of certain engines can be discontinuous or non-linear (Durdina et al., 2017; Boies et al., 2015), the four data points that are provided by the ICAO EDB are not sufficient to construct custom fits for each engine and account for these effects. Despite that, the EDB-interpolation approach is an improvement relative to existing methodologies that are currently used to estimate the nvPM EI_n and EI_m, such as the Smoke Correlation for Particle Emissions CAEP11 (SCOPE11) (Agarwal et al., 2019), Formation and Oxidation (FOX) (Stettler et al., 2013) and Improved FOX (Abrahamson et al., 2016) methods, because it captures differences in the distinct emissions profile for different engine/combustor types. The Fractal Aggregates (FA) model, on the other hand, estimates the nvPM EI_n from the EI_m (using FOX and ImFOX), particle size distribution and morphology; and EI_m estimates from the FOX and ImFOX methods were formulated based on the emissions profile of singular annular combustors (Teoh et al., 2020b, a, 2019).

S2.3 Example & Comparison

Several studies have measured the aircraft nvPM EI_n at cruise conditions (Voigt et al., 2021; Moore et al., 2017). Here, we use published data from Voigt et al. (2021) (Airbus A320, IAE-V2527-A5 engines) as a worked example to estimate the nvPM EI_n, and then compare it with the measured EI_n for conventional fuels. The operating condition and measured nvPM for the standard Jet A1 fuel scenario (Ref2) are provided below:

- Altitude = 10670 m; Pressure altitude, $P_{amb} \approx 23850$ Pa
- Ambient temperature, $T_{amb} = 215$ K
- Mach number = 0.65
- Fuel mass flow rate per engine = 1180 kg h^{-1} (0.328 kg s^{-1})
- Measured nvPM $EI_n = 4.9 \pm 0.6 \times 10^{15}$ kg^{-1} (1 S.D.)

The engine properties, fuel mass flow rate and emissions profile for an Airbus A320 (IAE V2527-A5) are extracted from the ICAO EDB:

- Engine pressure ratio, $\pi_{00} = 27.1$
- Fuel flow ($\dot{m}_f$) and nvPM EI_n (system loss corrected):

LTO Cycle	Idle	Approach	Climb out	Take-off
$\dot{\boldsymbol{m}}_{\mathbf{f}}$ (kg s^{-1})	0.134	0.328	0.873	1.049
$\left(\frac{T_4}{T_2}\right)_{\mathbf{Calculated}}$	2.1997	3.0173	4.37644	4.6987
nvPM EI_n ($\times 10^{15}$ kg^{-1})	6.93	7.45	3.34	2.56

The thermodynamic quantities that are required to estimate the non-dimensional engine thrust settings (T_4/T_2) are estimated with the equations listed in §S2.2:

Eq. (S1): $$\frac{F}{F_{00,\max}} = \frac{0.328}{1.049} = 0.3127$$

Eq. (S2): $P_2 = 23850\,(1 + \frac{0.4}{2} \times 0.65^2)^{\frac{1.4}{0.4}} = 36581.62$ Pa

Eq. (S3): $T_2 = 215\left(1 + \frac{0.4}{2} \times 0.65^2\right) = 233.17$ K

Eq. (S4): $P_3 = 36581.62 \times (27.1 - 1)(0.3127) + 36581.62 = 335121.12$ Pa

Eq. (S5): $T_3 = 233.17 \times (\frac{335121.12}{36581.62})^{\frac{0.4}{1.4(0.9)}} = 471.03$ K

Eq. (S7) & (S8): $\mathrm{AFR_{cruise}} = (0.0121(0.3127) + 0.008)^{-1} \times \left(\frac{233.17}{288.15}\right) = 68.672$

Eq. (S5): $T_4 = \frac{(68.672 \times 1005 \times 471.03) + (43.2 \times 10^6)}{1250\,(1 + 68.672)} = 868.13$ K

$$\left(\frac{T_4}{T_2}\right)_{\mathrm{Cruise}} = \frac{868.13}{233.17} = 3.723$$

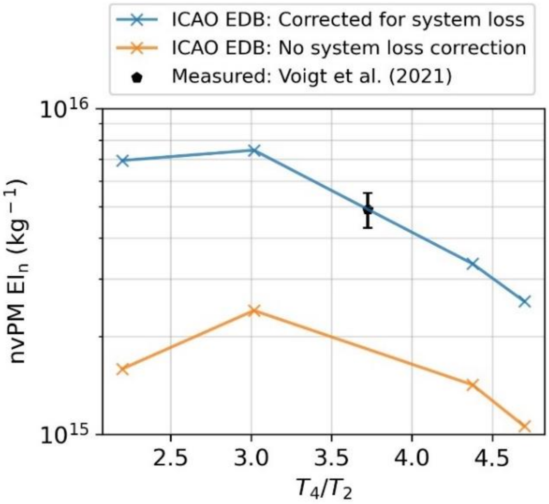

Figure S8: nvPM EI$_n$ emissions profile from the ICAO EDB and cruise EI$_n$ measurements from Voigt et al.(Voigt et al., 2021) **versus the non-dimensional engine thrust settings (T_4/T_2). The nvPM EI$_n$ is measured from an IAE V2527-A5 engine, which powers the Airbus A320.**

An interpolation of $\left(\frac{T_4}{T_2}\right)_{\mathrm{Cruise}}$ against values from the ICAO EDB estimates the nvPM EI$_n$ to be 5.32 $\times 10^{15}$ kg^{-1}. The estimated nvPM EI$_n$ (5.32 $\times 10^{15}$ kg^{-1}) is within the one standard deviation range of the measured EI$_n$ (4.9 ± 0.6 $\times 10^{15}$ kg^{-1}), as shown in Fig. S8. We note that the cruise nvPM EI$_n$ measurements from Moore et al. (2017) is not included in this validation because nvPM measurements from the engine type (DC-8, CFM56-2-C1) is not available in the ICAO EDB database.

S3 Correction to ERA5 humidity fields

In this study, contrails are simulated with two European Centre for Medium-Range Weather Forecast (ECMWF) ERA5 reanalysis datasets, including the high-resolution realization (ERA5 HRES) and 10-member ensembles. It is the ECMWF's fifth-generation reanalysis dataset and a successor to the ERA5-Interim reanalysis (Hersbach et al., 2020). The ERA5 HRES provides the nominal meteorology and radiation data at a very high spatiotemporal resolution (0.25° × 0.25° × 37 pressure levels × 1 h), while the ERA5 10-member ensembles has a lower spatiotemporal resolution (0.5° × 0.5° × 37 levels × 3 h) and is made up of: (i) one control member that is also used to initialise the HRES; and (ii) nine perturbed members where they are initialised with random perturbations added to the observations (Hersbach et al., 2020). Therefore, the ensemble spread that is provided by the ERA5 10-member ensembles represent uncertainties of the observing system that is provided to the data assimilation system and model state uncertainties in the reanalysis.

Existing studies have identified limitations of the humidity fields provided by the ECMWF ERA5 products: (i) it generally predicts ice supersaturated regions (ISSR) that are weakly supersaturated (RHi ≈ 100%); and (ii) do not predict regions with very high ice supersaturation (relative humidity with respect to ice, RHi > 120%) (Gierens et al., 2020; Schumann et al., 2021; Rädel and Shine, 2010; Reutter et al., 2020; Tompkins et al., 2007). Recent studies that compared the ERA5 humidity fields with in-situ measurements confirmed that the ERA5 products underpredict the RHi inside ISSRs (Reutter et al., 2020; Gierens et al., 2020), and two main factors likely contribute to this phenomenon: (i) the sub-grid scale variability that cannot currently be resolved from the spatiotemporal resolution of existing meteorological datasets; and (ii) simplified assumptions on the relaxation time, where all the supersaturated humidity in a grid cell is converted into ice, reaching equilibrium (RHi ≈ 100%) after one time step (Tompkins et al., 2007; Koop et al., 2000).

The identified limitations in the ERA5 humidity fields could lead to significant errors in the simulated contrail lifetime and climate forcing (Agarwal et al., 2022; Gierens et al., 2020). Previous studies that used the contrail cirrus prediction model (CoCiP) accounted for these limitations by uniformly increasing the ERA5 humidity fields by dividing it with an enhancement factor (RHi/RHi_c) with $RHi_c = 0.90$ (Schumann, 2012; Schumann et al., 2015; Teoh et al., 2020b) and $RHi_c = 0.95$ in Schumann et al. (2021), and differences in the RHi_c enhancement factor was attributed to different meteorological products and its spatiotemporal resolution. This approach of uniformly enhancing the ERA5 humidity fields ($RHi_c < 1$) can address limitation (i) by enhancing the mean RHi inside ISSRs; but it could overestimate the ISSR coverage and contrail formation (Agarwal et al., 2022), and does not reproduce an RHi distribution that is consistent with in-situ measurements(Schumann et al., 2021; Reutter et al., 2020).

Table S2: Comparison of the agreement in ISSR occurrence that is measured from the IAGOS campaign in 2019 versus those derived from the ERA5 HRES with a range of RHi_c factors. Y_{IAGOS} indicates that the waypoint is in ISSR (RHi > 100%) according to the in-situ IAGOS measurements, while N_{IAGOS} indicates the opposite. The same notations are used to assess the statistics for the ERA5 HRES.

RHic	**Y_{IAGOS}/Y_{HRES} (%)**	**N_{IAGOS}/N_{HRES} (%)**	**Y_{IAGOS}/N_{HRES} (%)**	**N_{IAGOS}/Y_{HRES} (%)**	**Equitable Threat Score (ETS)[a]**
0.90	**10.5**	**79.3**	**3.29**	**6.86**	0.444
0.91	10.3	79.7	3.48	6.48	0.446
0.92	10.2	80.1	3.64	6.15	0.447
0.93	9.94	80.4	3.86	5.82	0.445
0.94	9.74	80.7	4.06	5.50	0.444
0.95	**9.49**	**81.0**	**4.31**	**5.19**	0.440
0.96	9.22	81.4	4.58	4.80	0.437
0.97	8.93	81.8	4.87	4.45	0.432
0.98	8.57	82.1	5.23	4.12	0.422
0.99	8.20	82.4	5.60	3.79	0.411
1.00	**7.75**	**82.7**	**6.05**	**3.47**	0.394
1.01	7.04	83.2	6.76	3.04	0.365
1.02	6.45	83.6	7.35	2.62	0.343
1.03	5.87	83.9	7.93	2.26	0.318
1.04	5.38	84.3	8.42	1.89	0.298
1.05	4.96	84.6	8.84	1.61	0.280

[a]: The equitable threat score (ETS) is calculated based on Appendix A of Gierens et al.(Gierens et al., 2020). For interpretation, an ETS = 1 implies that all the in-situ IAGOS measurements matches up with the ERA5 HRES ($Y_{IAGOS}/Y_{HRES} + N_{IAGOS}/N_{HRES} = 100\%$); an ETS = 0 implies a completely random relationship between the IAGOS and ERA5 HRES; while an ETS < 0 implies an inverse relationship between the IAGOS and ERA5 HRES.

We used in-situ measurements from the In-Service Aircraft for a Global Observing System (IAGOS) campaign (Petzold et al., 2020; Boulanger et al., 2022) to develop a new correction methodology to address the identified limitations in the ERA5 humidity fields. For each flight, the IAGOS dataset measures the ambient temperature and humidity every 4 s, and we resampled the data to produce flight segments with a temporal resolution of 60 s to reduce autocorrelation in the atmospheric measurements (Gierens et al., 2020). We then filter the dataset to only include waypoints that are within the spatiotemporal domain of the NATS dataset (50°W, 40°N, 10°W, 75°N), and this amounted to 262 distinct flights and 43,919 waypoints for 2019. For each waypoint, the RHi is: (i) calculated from in-situ temperature and humidity measurements; and (ii) estimated from the ERA5 meteorology,

$$\mathrm{RHi} = \frac{q_{\mathrm{amb}} \times P_{\mathrm{amb}} \times \mathrm{R}_1}{p_{\mathrm{ice}}(T_{\mathrm{amb}}) \times \mathrm{R}_0}. \qquad \text{(S9)}$$

P_{amb} is the pressure altitude for each waypoint (in units of Pa), R_1 (461.51 J kg^{-1} K^{-1}) and R_0 (287.05 J kg^{-1} K^{-1}) are the real gas constant for water vapour and air respectively, and p_{ice} is the saturation pressure over ice water surfaces (Sonntag, 1994),

$$p_{\mathrm{ice}}[\mathrm{Pa}] = 100 \exp\left[\frac{-6024.5282}{T_{\mathrm{amb}}} + 24.721994 + 0.010613868 T_{\mathrm{amb}} - 1.3198825 \times 10^{-5} {T_{\mathrm{amb}}}^2 - 0.49382577 \ln(T_{\mathrm{amb}})\right], \qquad \text{(S10)}$$

where q_{amb} is the specific humidity (kg-H_2O/kg-air) and T_{amb} is the ambient temperature, and a quadrilinear interpolation provides the q_{amb} and T_{amb} from the ERA5 datasets.

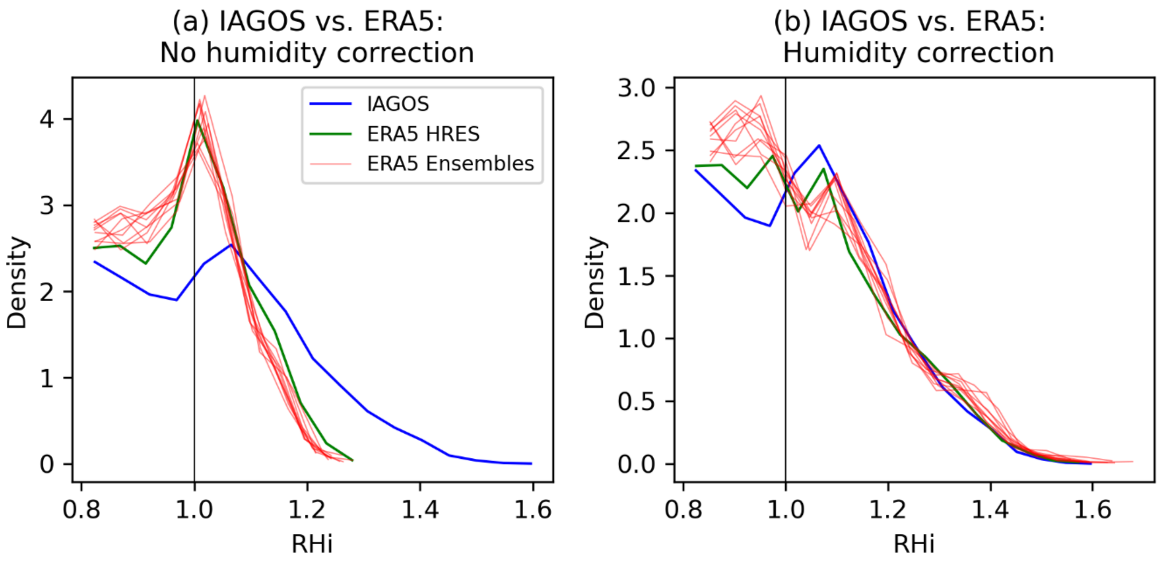

Figure S9: Probability density function of the RHi for the IAGOS waypoints that is calculated from in-situ temperature and humidity measurements versus those estimated from the ERA5 HRES and ERA5 10-member ensembles (a) without and (b) with humidity correction.

Two approaches are used to compare the goodness of fit between the in-situ and ERA5-derived RHi, including the ability for the ERA5 products to correctly predict: (i) the location of ISSRs (RHi ≥ 100%) and dry regions (RHi < 100%), which determines contrail formation; and (ii) the RHi magnitude inside ISSRs, which influences the contrail properties, lifetime, and climate forcing. Table S2 summarises the ability of ERA5 HRES to correctly predict the waypoints inside/outside ISSRs versus a range of RHi_c enhancement factors that covers the values used in previous studies; while Fig. S9a compares the RHi distribution from the ERA5 HRES with no humidity correction with in-situ measurements. Without applying any humidity correction ($RHi_c = 1$), our results show that:

1. the ERA5 HRES correctly predicts the formation/absence of contrails for 90.5% of the IAGOS waypoints in the sample (Table S2),
2. the false negative rate (Y_{IAGOS}/N_{HRES}, where IAGOS indicates ISSR, but not in the ERA5 humidity fields) is 1.8 times higher than the false positive rate (N_{IAGOS}/Y_{HRES}, where ERA5 indicates ISSR, but not the IAGOS measurements), at 6.05% versus

3.47% (Table S2), which suggests that the uncorrected ERA5 could underestimate the ISSR occurrence,

3. RHi derived from the ERA5 HRES shows a peak at around 105% RHi and do not exceed 125% RHi, while the RHi derived from in-situ measurements more closely resembles a negative exponential/power-law distribution with RHi values of up to 160% (Fig. S9a), and
4. Applying a uniform enhancement factor of up to RHi_c < 0.92 can improve the agreement between the IAGOS and ERA5, as indicated by the Equitable Threat Score (ETS). However, applying an RHic < 0.96 to the North Atlantic region causes the false positive rate (N_{IAGOS}/Y_{HRES}) to be greater than the false negative rate (Y_{IAGOS}/N_{HRES}), potentially overestimating the contrail formation, persistence, and climate forcing (Table S2).

These results are consistent with earlier studies which found the ERA5 HRES to generally predict ISSR regions that are weakly supersaturated (RHi ≈ 100%) (Gierens et al., 2020; Schumann et al., 2021; Rädel and Shine, 2010; Reutter et al., 2020; Tompkins et al., 2007); and the potential underestimation of ISSR occurrence, highlighted in Point (2), is in contrast to a recent study that compared the ERA5 RHi with radiosonde measurements (Agarwal et al., 2022).

Based on these results, we developed a new approach to correct the ERA5 humidity fields:

- **STEP 1**: Scale the ERA5 humidity fields in the spatial domain by dividing by a factor of *a*,
- **STEP 2**: Enhance the RHi of any data points with ISSRs (RHi > 100%) using a power-law function with coefficient *b* and limit the RHi to an upper bound of 165%, in-line with observations from the IAGOS dataset.

$$\mathrm{RHi}_{\mathrm{Corrected}} = \begin{cases} \dfrac{\mathrm{RHi}}{a} & \text{, when } \left(\dfrac{\mathrm{RHi}}{a}\right) \leq 1 \\ \min\left(\left(\dfrac{\mathrm{RHi}}{a}\right)^{b}, 1.65\right) & \text{, when } \left(\dfrac{\mathrm{RHi}}{a}\right) > 1 \end{cases} \qquad \text{(S11)}$$

The parameters a and b are optimised by minimising the Cramer-von Mises (CvM) test statistic (Parr and Schucany, 1980), a measure of the goodness-of-fit between two empirical distributions, so that the probability density function of the ERA5-derived RHi inside ISSRs (RHi > 100%) resembles the IAGOS in-situ measurements,

$$T = \frac{1}{12n} + \sum_{i=1}^{n} \left[\frac{2i-1}{2n} - F(x_i)\right]^2, \qquad \text{(S12)}$$

where n is the sample size and $F(x_i)$ is the cumulative density function of the sample (ERA5 RHi) calculated relative to the distribution of in-situ measurements from IAGOS, with values ranging between 0 and 1. A lower T value indicates an improved goodness-of fit(Parr and Schucany, 1980), and this approach improves the robustness of the test relative to the more commonly used Kolmogorov-Smirnov test because it accounts for the whole distribution function.

Using the SciPy Python package, we estimate $a = 0.9779$ and $b = 1.635$ for the ERA5 HRES. Figure S10a shows the CvM test statistic against a range of b values for the ERA5 HRES and shows that the optimal b value (1.635) is a global minimum. We note that the optimised a and b coefficients are specific for the North Atlantic region and might not be valid for other regions. After correcting the humidity fields, the RHi distribution provided by the ERA5 HRES now resembles the IAGOS in-situ measurements (Fig. S9b). Figure S11 compares the spatial distribution of the ERA5 humidity fields before and after applying the humidity correction, as well as previous approaches that corrected the humidity fields by division with a uniform enhancement factor of RHi_c: the new correction approach maintains the ISSR structure, and it now accounts for regions with very high ice supersaturation (RHi > 120%). In contrast, the previous correction approaches (RHi_c = 0.90 and 0.95) do not adequately capture localised regions with very high RHi, and the larger ISSR coverage area (RHi_c < 0.96) could overestimate the contrail formation and climate forcing (Table S2).

The same humidity correction approach is applied to the ERA5 10-member ensembles. Without applying any correction, we found that the RHi derived from the ERA5 10-member ensembles is, on average, 2.5% lower than the ERA5 HRES, which can likely be attributed to its lower spatiotemporal resolution. The optimal a and b coefficients are then estimated for each ensemble member, and we applied the median coefficients to all the ensemble members ($a = 0.9666$ and $b = 1.776$). Figure S9b shows the RHi distribution inside ISSRs after the humidity correction is applied to the ERA5 10-member ensembles, which now resembles the IAGOS in-situ measurements.

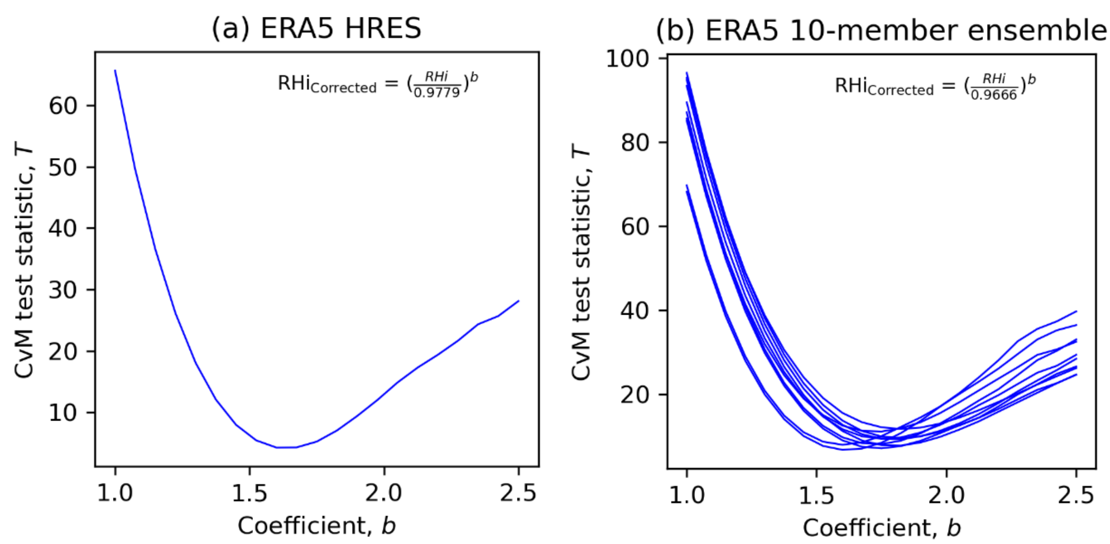

Figure S10: The CvM test statistic versus a range of *b* coefficient that is used in Eq. (S11) to correct for the humidity fields in the (a) ERA5 HRES; and (b) ERA5 10-member ensembles.

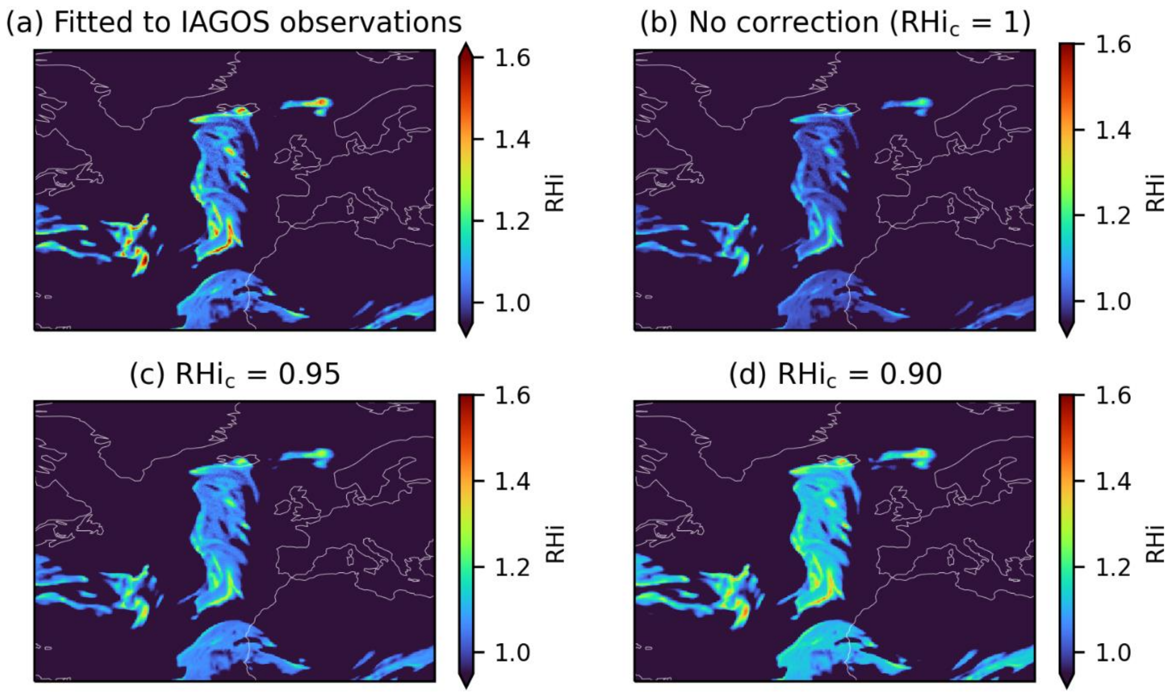

Figure S11: Spatial distribution of the humidity fields from the ERA5 HRES (a) with and (b) without humidity correction; and for previous approaches that uniformly enhanced the humidity fields by dividing with (c) RHi$_c$ = 0.95; and (d) RHi$_c$ = 0.90 at pressure level 20,000 Pa (38,500 feet) and 2-January-2019 20:00:00 (UTC). Basemap plotted using Cartopy 0.20.2 (C) Natural Earth; license: public domain.

Table S3: Comparison of the agreement in ISSR occurrence that is measured from the IAGOS campaign in 2019 versus those derived from the median of the ERA5 10-member ensembles with a range of RHi$_c$ boosting factors. Y_{IAGOS} indicates that the waypoint is in ISSR (RHi > 100%) according to in-situ IAGOS measurements, while N_{IAGOS} indicates the opposite. The same notations are used to assess the statistics for the ERA5 10-member ensembles.

RHic	Y_{IAGOS}/Y_{ENS} (%)	N_{IAGOS}/N_{ENS} (%)	Y_{IAGOS}/N_{ENS} (%)	N_{IAGOS}/Y_{ENS} (%)	Equitable Threat Score (ETS)[a]
0.90	**10.1**	**79.3**	**3.67**	**6.93**	0.423
0.91	9.89	79.7	3.91	6.51	0.422
0.92	9.62	80.1	4.18	6.14	0.419
0.93	9.35	80.5	4.45	5.75	0.416
0.94	9.07	80.9	4.73	5.34	0.413
0.95	**8.78**	**81.2**	**5.02**	**4.96**	0.408
0.96	8.45	81.6	5.35	4.60	0.401
0.97	8.12	82.0	5.68	4.21	0.394
0.98	7.76	82.4	6.04	3.83	0.384
0.99	7.39	82.8	6.41	3.41	0.376
1.00	**6.96**	**83.2**	**6.84**	**2.99**	0.363
1.01	6.37	83.6	7.43	2.60	0.338
1.02	5.73	84.0	8.08	2.16	0.312
1.03	5.11	84.4	8.69	1.83	0.283
1.04	4.54	84.6	9.26	1.56	0.255
1.05	3.96	84.9	9.84	1.32	0.225

[a]: The equitable threat score (ETS) is calculated based on Appendix A of Gierens et al.(Gierens et al., 2020). For interpretation, an ETS = 1 implies that all the in-situ IAGOS measurements matches up with the median of the ERA5 10-member ensembles (Y_{IAGOS}/Y_{ENS} + N_{IAGOS}/N_{ENS} = 100%); an ETS = 0 implies a completely random relationship between the IAGOS and ERA5 ensembles; while an ETS < 0 implies an inverse relationship between the IAGOS and ERA5 ensembles.

Table S4 shows the agreement of the ISSR occurrence between the IAGOS in-situ measurements versus those derived from the corrected ERA5 humidity fields, while Fig. S9 shows the corrected RHi distribution relative to in-situ measurements. While the new humidity correction approach is an improvement relative to previous approaches, we acknowledge its inherent limitations where: (i) the optimal coefficients for *a* and *b* are only valid for the North Atlantic region; and (ii) it could introduce errors at an individual waypoint level because the optimisation was performed using the probability density function. Recent studies found that that the accuracy of ERA5-derived RHi has a seasonal and height dependence (Gierens et al., 2020; Reutter et al., 2020), and further research is currently ongoing among the community to quantify these uncertainties and explore various machine-learning techniques to improve the accuracy of the ERA5 humidity fields.

Table S4: Comparison of the agreement in ISSR occurrence that is measured from the IAGOS campaign in 2019 versus those derived from the ERA5 HRES and 10-member ensembles where the humidity fields are corrected using Eq. (S11).

ERA5 Product	Coefficients		YIAGOS/YERA5 (%)	NIAGOS/NERA5 (%)	NIAGOS/NERA5 (%)	NIAGOS/NERA5 (%)	ETS
	a	*b*					
HRES	0.9779	1.635	8.64	82.0	5.16	4.19	0.424
10-member Ensembles	0.9666	1.776	8.23	81.8	5.57	4.36	0.395

S4 Conditions for forming strongly warming/cooling contrails

The contrail cirrus net RF exhibits significant year-on-year variability with a stronger dependence on meteorology than on the total flight distance (Fig. S12). Figure S13 shows the seasonal variations in the ISSR properties, which is a key factor contributing to seasonal variations in different contrail properties (Fig. 1, 3 and 4 in the main text, and Fig. S14). Figure S15 shows a large intersection between the ISSR and the North Atlantic Organised Track Structure (OTS) at 17-April-2017, which contributes to the outliers observed in the seasonal contrail statistics (Fig. 1 in the main text) around that time period.

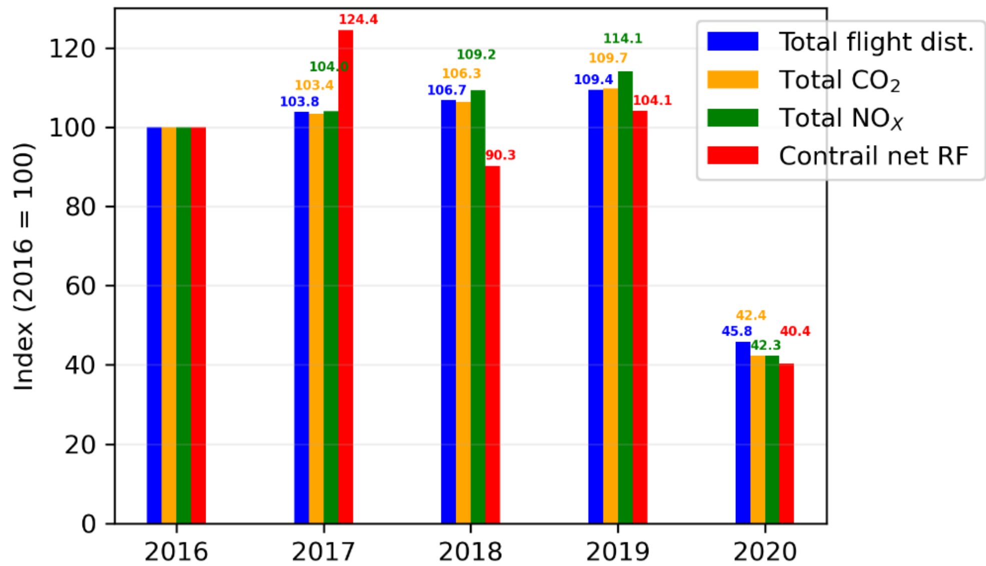

Figure S12: The annual air traffic distance travelled, CO_2 and NO_x emissions, and the contrail cirrus net RF in the North Atlantic region between 2016 and 2020, all of which are indexed to the 2016 values.

Figure 3a (main text) shows the diurnal and seasonal effect of the contrail cirrus net RF, and large variabilities in the daytime contrail cirrus net RF is observed where it can be strongly warming (1086 mW m^{-2}, 18-Sept-2019 14:00 UTC) or cooling (-594 mW m^{-2}, 28-Aug-2019 10:00). For both periods, there is a contrail outbreak over the ocean (Fig. S16 left). Around 76.2% and 68.2% of the contrail area overlaps with natural cirrus in the warming and cooling period respectively (Fig. S16 right). A comparison of the local meteorology and various contrail properties in both the warming and cooling periods are shown as a probability density function in Fig. S17.

Figure S18 shows that the mean contrail ice crystal radius (r_{ice}) is correlated with the initial RHi (R = 0.661), the difference between the ambient and SAC threshold temperature (dT_{SAC}) (R = 0.551), contrail optical depth (τ_{contrail}) (R = 0.585), and negatively correlated with the contrail age (R = -0.350). Figure S19 provides a breakdown of the aircraft types that are responsible for strongly warming (EF_{contrail} > 99$^{\mathrm{th}}$ percentile) and cooling (EF_{contrail} < 1$^{\mathrm{st}}$ percentile) contrails. It shows that 43.4% (17.4%) of strongly warming (cooling) contrails are formed by aircraft powered by the Phase 5 Rich-Quench-Lean combustor, and a very large wide-body aircraft is responsible for 18.0% (6.4%) of flights with strongly warming (cooling) contrails. Table S5 shows the relative contribution of different aircraft types to the contrail climate forcing.

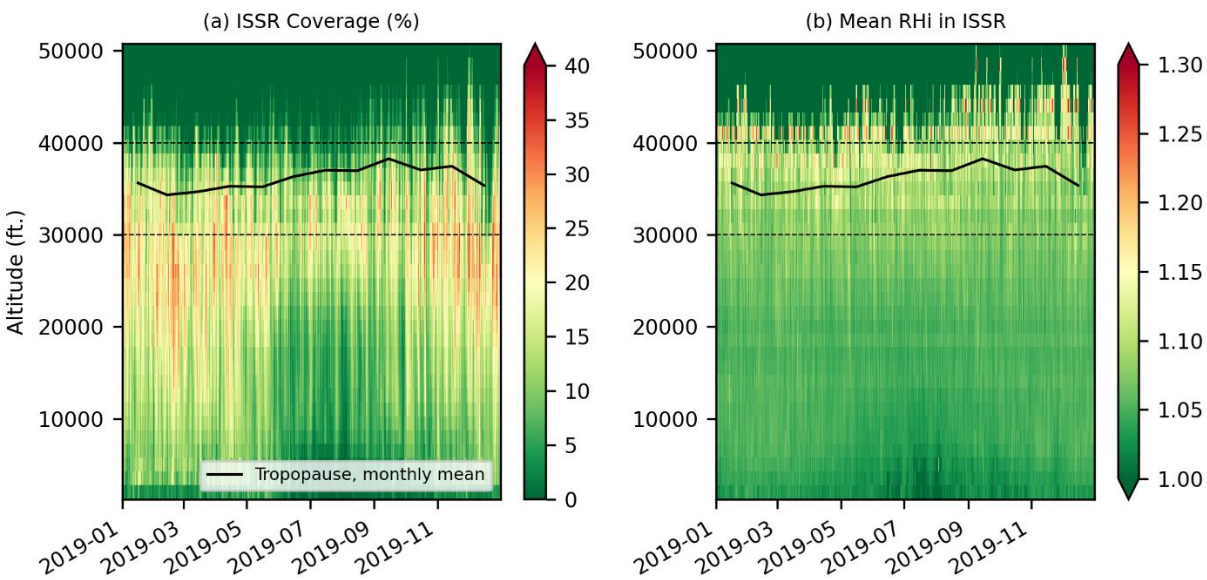

Figure S13: ISSR properties vs. altitude in the North Atlantic region for 2019, including: (a) the percentage of coverage area, i.e., regions where the RHi > 1; and (b) the mean RHi in the ISSRs. The data is provided by the ERA5 HRES dataset. The black lines represent the monthly mean tropopause height calculated using the World Meteorological Organization (WMO) criteria where the lapse rate stays above -2 K km^{-1}, and the black horizontal dashed lines represent the typical cruising altitudes of between 9 and 12 km.

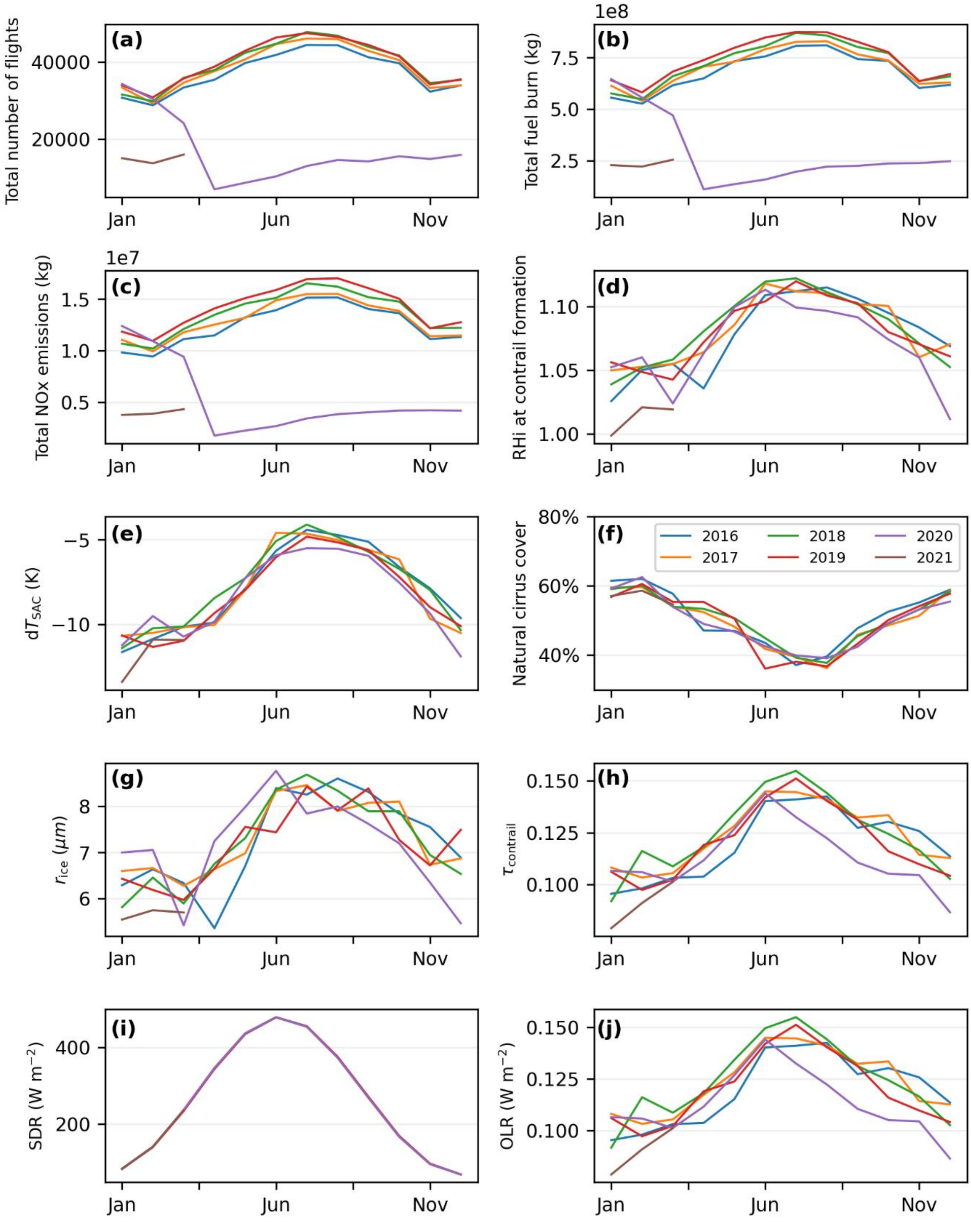

Figure S14: Monthly statistics in the North Atlantic region from January-2016 to March-2021, including the (a) total number of flights; (b) total fuel consumption; (c) total NO_x emissions; (d) mean RHi when the contrail is formed; (e) mean differences between the ambient and Schmidt-Appleman criterion threshold temperature (dT_{SAC}); (f) natural cirrus coverage; (g) mean ice crystal radius (r_{ice}); (h) mean contrail optical depth ($\tau_{contrail}$); (i) mean solar direct radiation (SDR); and (j) mean outgoing longwave radiation (OLR).

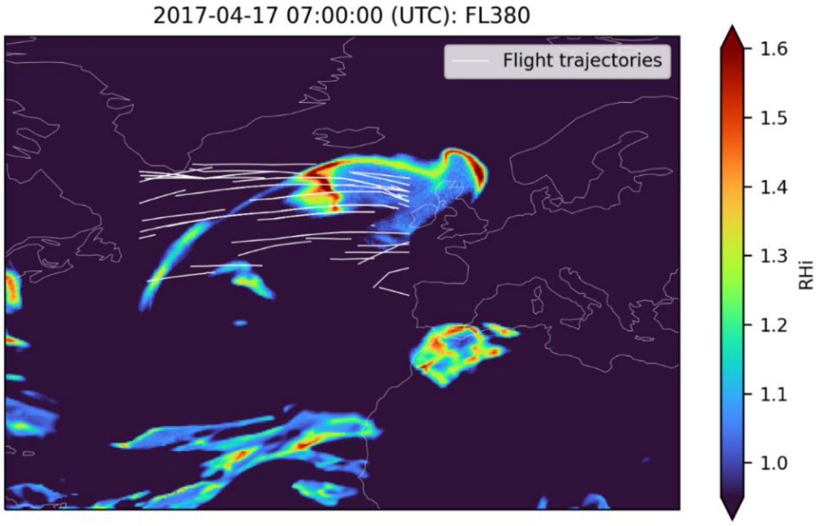

Figure S15: Spatial distribution of the corrected ERA5 humidity fields at flight level 380 (38,000 feet), 17-April-2017 07:00:00 (UTC). The white lines represent the flight trajectories that traversed the airspace in between 06:30:00 and 07:30:00 (UTC). During this time, 54% of the flight distance formed contrails and the contrail cirrus net RF is 1430 mW m^{-2}, which are shown as outliers in Fig. 2 (main text), and this is caused by the large intersection between the ISSR and the North Atlantic Organised Track Structure. Basemap plotted using Cartopy 0.20.2 (C) Natural Earth; license: public domain.

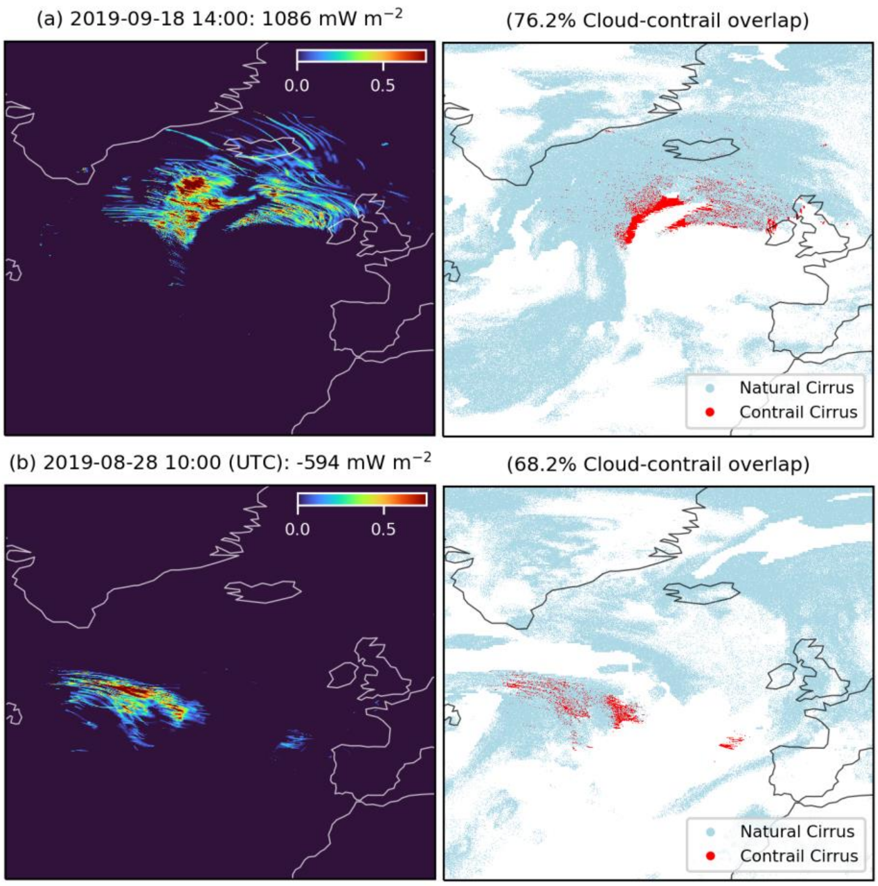

Figure S16: Gridded contrail cirrus optical depth ($\tau_{contrail}$) under clear sky conditions (left) and the location of natural cirrus and contrail cirrus (right) for the: (a) warming period at 18-Sept-2019 14:00 (UTC); and (b) cooling period at 28-Aug-2019 10:00. The contrail cirrus coverage (red points in the right subplots) are contrails that do not overlap with natural cirrus (refer to Section 2.5). Basemap plotted using Cartopy 0.20.2 (C) Natural Earth; license: public domain.

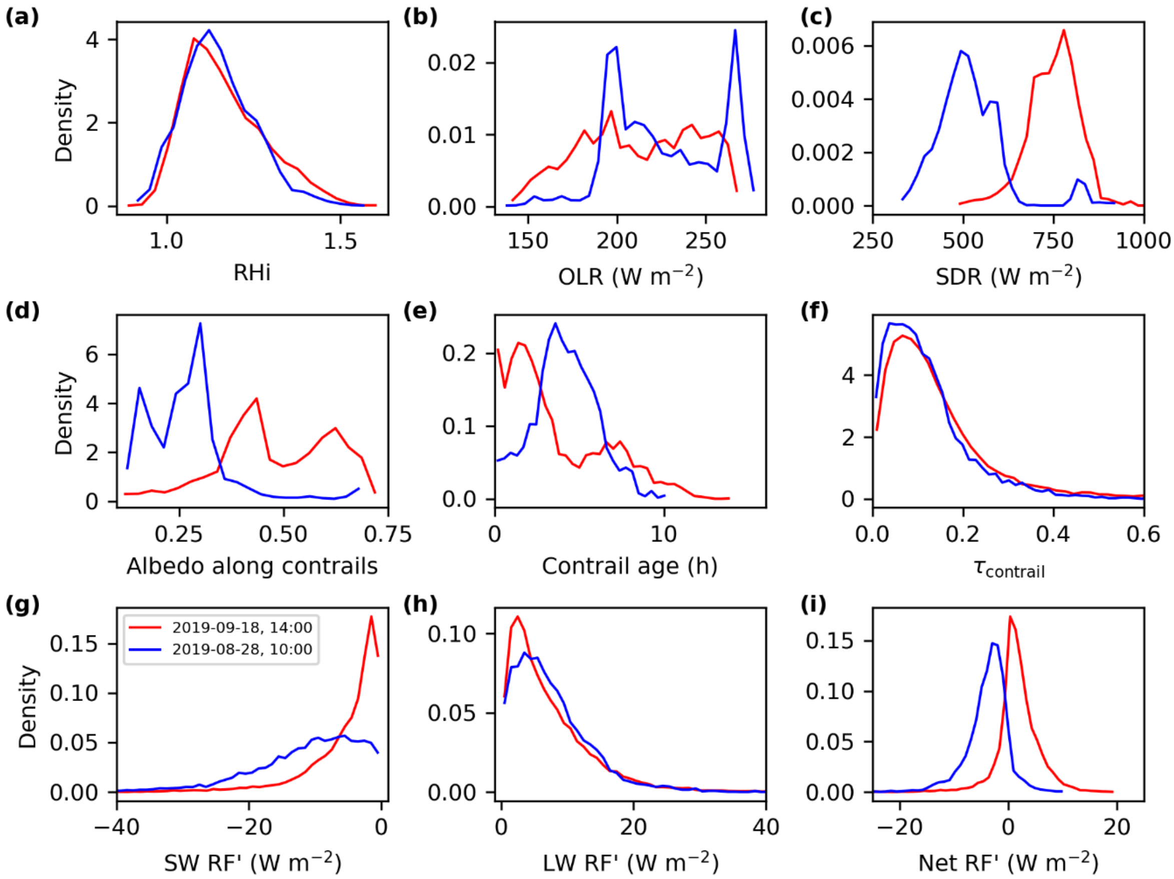

Figure S17: Probability density function for the local meteorology, radiation and contrail properties at the contrail waypoint level during the warming period at 18-Sept-2019 14:00 UTC (red lines) and the cooling period at 28-Aug-2019 10:00 (green lines).

S5 Uncertainty analysis

Uncertainties provided by the ERA5 10-member ensembles are propagated to estimates of the annual emissions and contrail properties for 2019. Table S6 summarises the 2019 air traffic, emissions, and contrail statistics for each of the ERA5 10-member ensembles. The properties of flights with strongly warming ($EF_{contrail}$ > 99th percentile for 2019) and cooling ($EF_{contrail}$ < 1st percentile) contrails derived from each ensemble member is presented in Fig. S20. The probability density functions are generally consistent with the nominal simulation (Fig. 4 in the main text), apart from the time of day where strongly warming/cooling contrails are formed.

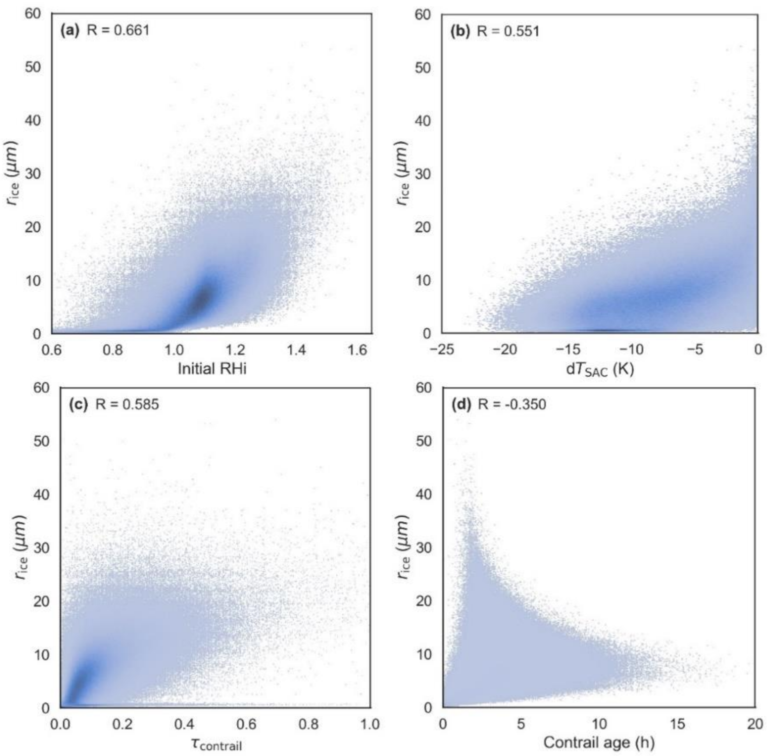

Figure S18: Correlation between the mean ice crystal radius (r_{ice}) versus the mean: (a) initial RHi at contrail formation; (b) difference between the ambient and SAC threshold temperature (dT_{SAC}); (c) contrail optical depth ($\tau_{contrail}$); and (d) contrail age for all contrail-forming flights.

Table S5: Statistics on the relative contribution of different aircraft types (annonymised) and their respective nvPM number emissions to the contrail climate forcing.

Aircraft Type	% of all flights	% strongly warming contrails[a]	% strongly cooling contrails[a]	Mean nvPM number per distance travelled ($\times10^{12}$ m^{-1})[b]	$EF_{contrail}$ per flight distance ($\times10^{8}$ J m^{-1})	$EF_{contrail}$ per passenger-km ($\times10^{5}$ J m^{-1})[c]
Medium wide body (AC1)	7.8%	6.3%	3.7%	5.18	0.90	4.86
Medium wide body (AC2)	11.1%	14.4%	12.3%	8.95	1.13	5.46
Large wide body (AC3)	1.7%	0.9%	2.4%	6.48	0.87	4.18
Large wide body (AC4)	1.6%	5.1%	2.1%	11.9	1.58	6.09
Large wide body (AC5)	1.3%	2.5%	0.8%	10.1	1.29	5.30
Large wide body (AC6)	0.4%	0.5%	0.2%	9.42	1.21	4.42
Very large wide body (AC7)	2.4%	18.0%	6.4%	24.0	2.18	4.51
Very large wide body (AC8)	7.4%	9.8%	9.6%	6.57	1.05	4.07
Very large wide body (AC9)	1.9%	0.0%	0.7%	2.97	0.50	1.64
Narrow body (AC10)	4.2%	0.8%	3.9%	5.39	0.71	4.86
Medium wide body (AC11)	10.9%	8.7%	24.2%	8.32	1.02	5.91
Very large wide body (AC12)	10.6%	4.2%	4.9%	4.33	0.79	3.33
Very large wide body (AC13)	3.2%	0.7%	2.1%	4.92	0.77	3.25
Very large wide body (AC14)	8.8%	2.1%	10.0%	5.17	0.73	2.46
Medium wide body (AC15)	4.8%	6.9%	1.9%	7.47	1.22	6.72
Medium wide body (AC16)	6.9%	9.4%	4.5%	8.36	1.18	5.40
Large wide body (AC17)	1.0%	2.5%	3.9%	14.9	1.01	4.53
Medium wide body (AC18)	0.6%	0.0%	0.0%	2.57	0.50	2.04

[a]: Flights with strongly warming and cooling contrails are defined as contrail-forming flights with $EF_{contrail}$ > 99th percentile and $EF_{contrail}$ < 1st percentile respectively.

[b]: nvPM number emissions per distance travelled = nvPM EI_n × fuel consumption per distance travelled

[c]: The $EF_{contrail}$ per passenger km is calculated by assuming a load factor of 75%.

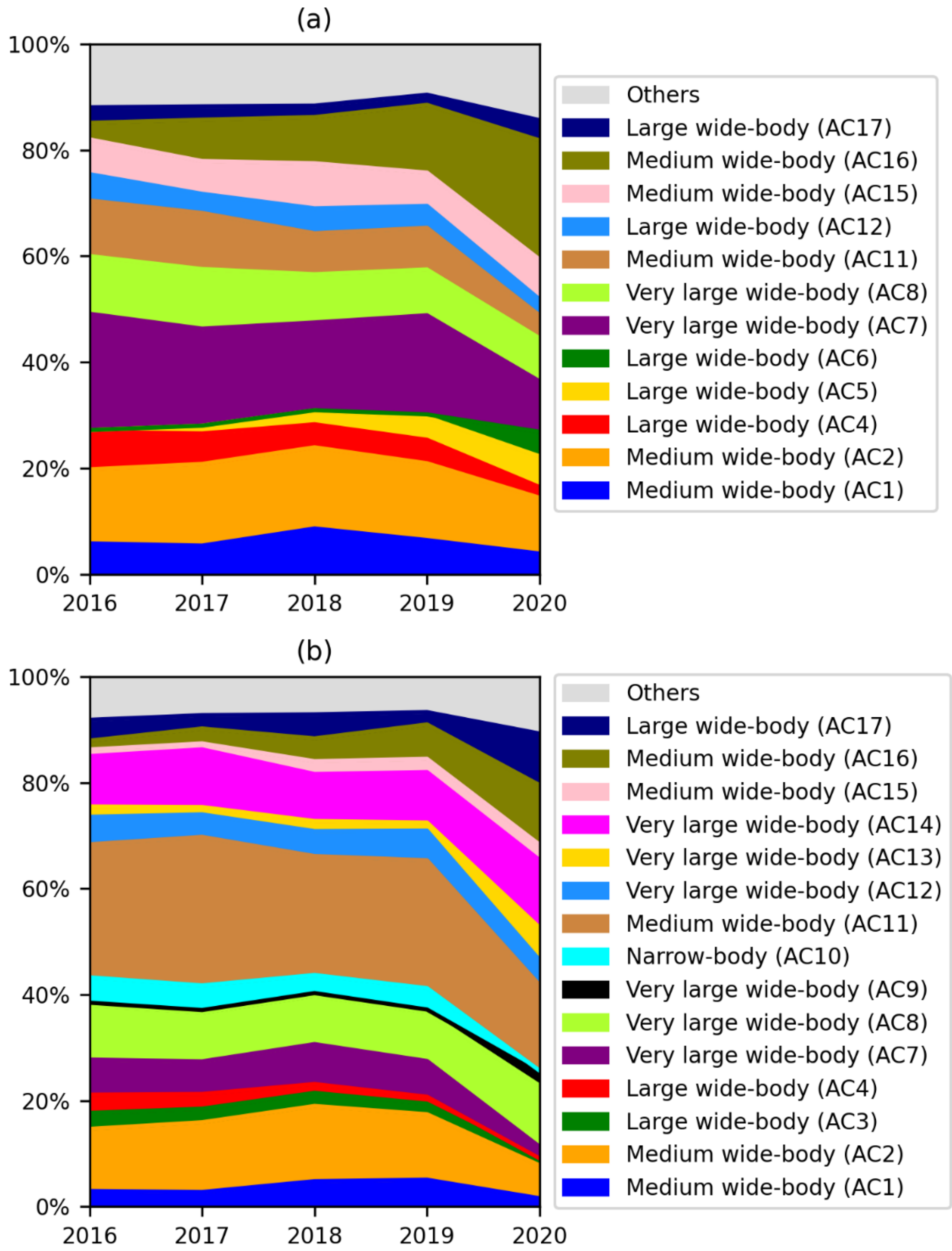

Figure S19: Breakdown of the aircraft types that are responsible for strongly warming ($EF_{contrail}$ > 99th percentile) and cooling ($EF_{contrail}$ < 1st percentile) contrails that were formed in the North Atlantic region between 2016 and 2020.

Table S6: The annual air traffic, emissions, and contrail statistics for each of the ERA5 10-member ensembles for 2019

2019 Ensemble members	**1**	**2**	**3**	**4**	**5**	**6**	**7**	**8**	**9**	**10**
Total number of flights	477923	477923	477923	477923	477923	477923	477923	477923	477923	477923
Total flight distance ($x10^9$ km)	1.184	1.184	1.184	1.184	1.184	1.184	1.184	1.184	1.184	1.184
Total fuel burn ($x10^9$ kg)	8.916	8.916	8.916	8.916	8.916	8.916	8.916	8.916	8.916	8.916
Mean overall propulsion efficiency, η	0.3252	0.3252	0.3252	0.3252	0.3252	0.3252	0.3252	0.3252	0.3252	0.3252
Total CO_2 emissions ($x10^9$ kg)	28.164	28.166	28.166	28.165	28.166	28.165	28.165	28.166	28.166	28.165
Total NO_x emissions ($x10^9$ kg)	0.1699	0.1700	0.1700	0.1699	0.1700	0.1699	0.1700	0.1700	0.1699	0.1699
Mean nvPM EI_n ($x10^{15}$ kg^{-1})	0.9393	0.9392	0.9392	0.9392	0.9392	0.9392	0.9392	0.9392	0.9392	0.9392
Flights forming persistent contrails (%)	52.47	52.56	52.50	52.45	52.49	52.41	52.29	52.37	52.35	52.38
Dist. forming persistent contrails (%)	16.45	16.16	16.19	16.14	16.17	16.10	16.07	16.07	16.07	16.10
Mean contrail age (h)	3.880	3.773	3.788	3.777	3.783	3.781	3.770	3.764	3.781	3.775
Contrail optical depth, τ	0.1292	0.1242	0.1250	0.1244	0.1241	0.1237	0.1243	0.1241	0.1245	0.1235
Contrail cirrus coverage (%)	0.551	0.536	0.538	0.529	0.539	0.526	0.531	0.537	0.533	0.536
SW RF (mW m^{-2})	-331.4	-307.2	-308.9	-303.8	-307.9	-304.9	-303.7	-307.4	-304.3	-305.4
LW RF (mW m^{-2})	569.3	527.4	529.8	523.0	526.7	523.4	519.3	525.4	521.2	525.8
Net RF (mW m^{-2})	237.8	220.2	220.9	219.2	218.8	218.5	215.6	217.9	216.9	220.4
$EF_{contrail}$ ($x10^{18}$ J)	63.62	58.84	59.04	58.61	58.46	58.42	57.68	58.29	58.02	58.97
$EF_{contrail}$ per flight distance ($x10^8$ J m^{-1})	0.5375	0.4971	0.4988	0.4952	0.4939	0.4936	0.4874	0.4925	0.4902	0.4982
$EF_{contrail}$ per contrail length ($x10^8$ J m^{-1})	3.267	3.077	3.080	3.068	3.055	3.065	3.032	3.064	3.050	3.094
% flights responsible for 80% $EF_{contrail}$	8.87	8.57	8.69	8.64	8.59	8.57	8.58	8.56	8.59	8.64

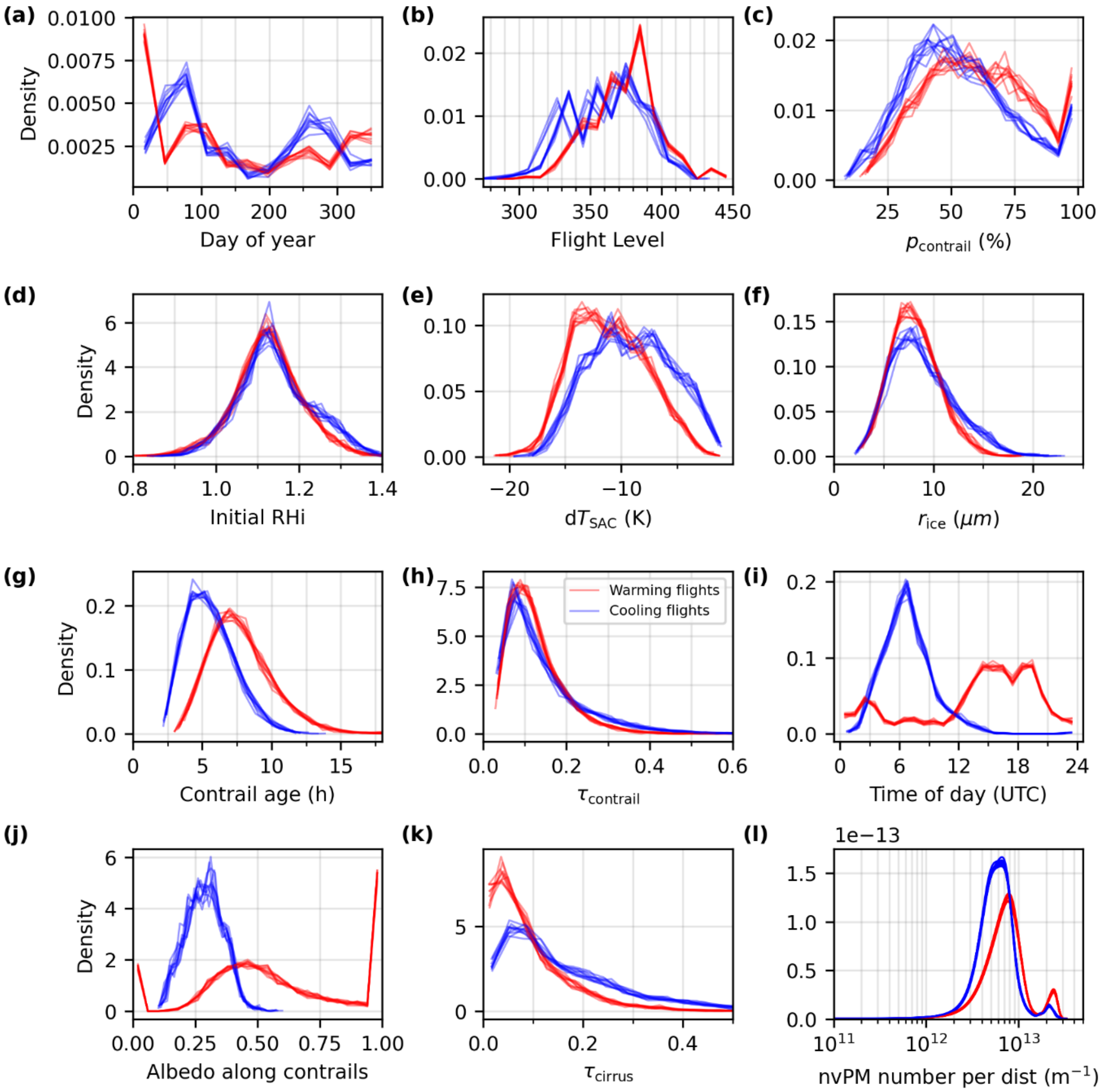

Figure S20: Probability density function of the aircraft, meteorology, and contrail properties for flights with highly warming (red lines, $EF_{contrail}$ > 99th percentile) and cooling contrails (blue lines, $EF_{contrail}$ < 1st percentile) that is derived from the ERA5 10-member ensembles for 2019. Each line represents the probability density function from each ensemble member. The time-of-day variable in panel (i) represents the time when the flight is at its midpoint between the first and final recorded waypoints.

S6 Sensitivity analysis

Sensitivity analyses are also performed to compare the difference in mean contrail properties from individual flights between the nominal simulation versus: (i) a model run without the humidity correction applied to the ERA5 HRES (Fig. S21); (ii) a constant EI_n scenario of assuming 10^{15} kg^{-1} for all waypoints (Fig. S22); and (iii) the assumption where all the nvPM activates into contrail ice crystals ($p_{\mathrm{activation}}$ = 1, Eq. 2 in the main text), independent of the ambient temperature (Fig. S23). Table S7 summarises the change in emissions, meteorology and contrail statistics for the different model runs used in the sensitivity analysis. The results show that the contrail outputs are most sensitive to the ERA5 humidity correction, followed by the nvPM EI_n, and is least sensitive to $p_{\mathrm{activation}}$. Figure S24 compares the mean contrail lifetime versus the mean RHi throughout the contrail's lifetime between the simulation with and without humidity correction. The humidity correction (described in §S3) accounts for regions with very high ice supersaturation (RHi > 120%), and contrails that persist under these conditions generally have shorter lifetimes because of a larger r_{ice} and sedimentation rate.

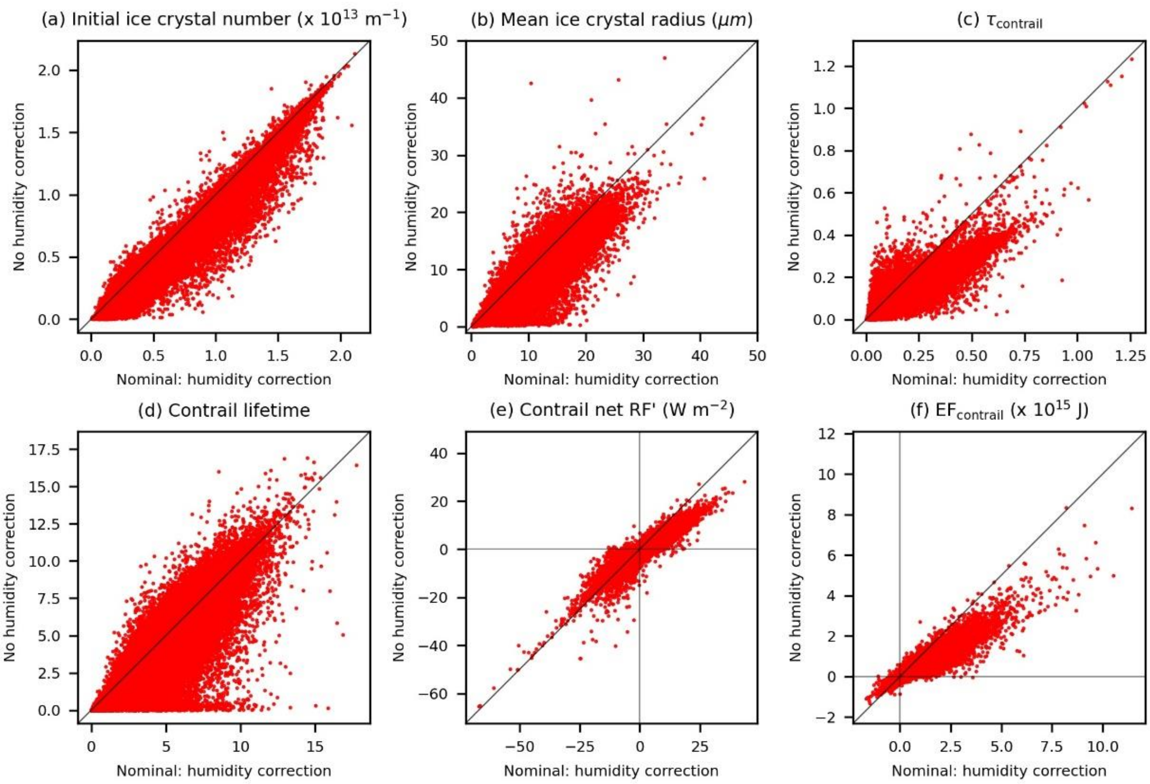

Figure S21: Parity plots comparing the difference in contrail properties between the nominal simulation (ERA5 HRES with humidity correction) versus model run without humidity correction. Each data point represents the mean contrail properties for one flight, and flights are only included in this comparison if contrails are formed in both model runs (n = 253,654).

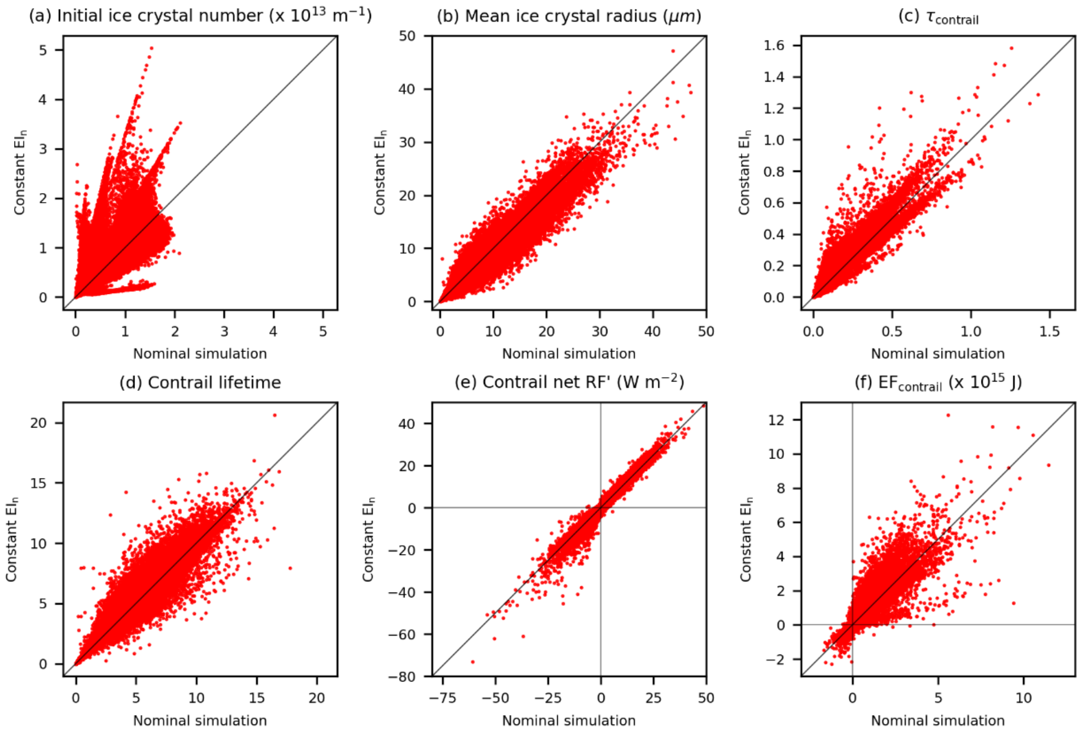

Figure S22: Parity plots comparing the difference in contrail properties between the nominal simulation (ERA5 HRES) versus a constant EI$_n$ scenario (10^{15} kg^{-1} for all waypoints). Each data point represents the mean contrail properties for one flight, and all contrail-forming flights in 2019 are included in this comparison (n = 266,829).

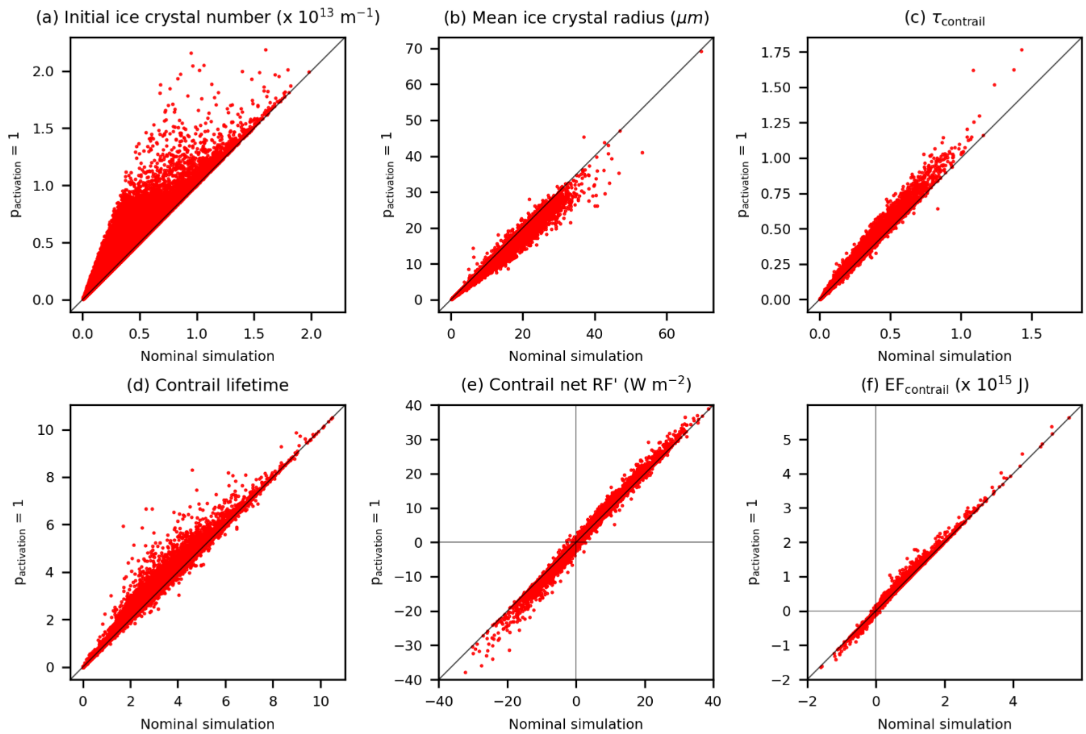

Figure S23: Parity plots comparing the difference in contrail properties between the nominal simulation (ERA5 HRES) versus the assumption where all the nvPM activates into contrail ice crystals ($p_{activation}$ = 1). Each data point represents the mean contrail properties for one flight, and only flights in 2019 that form contrails near the Schmidt-Appleman threshold ($T_{amb} - T_{SAC}$ > -5 K) are included in this comparison (n = 66,297).

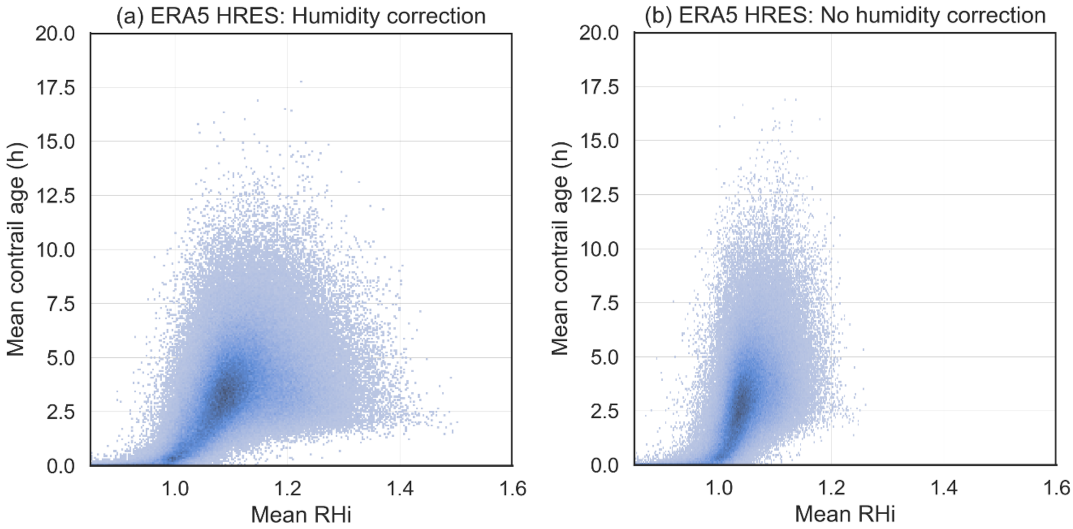

Figure S24: The simulated mean contrail age versus the mean RHi throughout the contrail's lifetime for all contrail-forming flights over the North Atlantic in 2019: (a) with; and (b) without humidity correction being applied to the ERA5 HRES.

Table S7: The 2019 air traffic, emissions, meteorology and contrail statistics in the North Atlantic region for the different model runs used in the sensitivity analysis.

Annual statistics	Sensitivity analysis: 2019					
	Nominal	**No RHi correction**	**Constant nvPM EI_n**	**Full nvPM activation**	**High aircraft mass**	**Low aircraft mass**
Total number of flights	477923	477923	477923	477923	477923	477923
Total flight distance ($x10^9$ km)	1.184	1.184	1.184	1.184	1.184	1.184
Total fuel burn ($x10^9$ kg)	8.922	8.922	8.922	8.922	9.992	7.475
Fuel burn per distance (kg km^{-1})	7.535	7.535	7.535	7.535	8.439	6.313
Mean aircraft mass (kg)	207793	207793	207793	207793	225931	177612
Mean overall propulsion efficiency, η	0.3252	0.3252	0.3252	0.3252	0.3234	0.3271
Total CO_2 emissions ($x10^9$ kg)	28.18	28.18	28.18	28.18	31.56	23.61
Total NO_x emissions ($x10^9$ kg)	0.1703	0.1703	0.1703	0.1703	0.2130	0.1192
Total nvPM number ($x10^{24}$)	8.379	8.379	8.922	8.379	8.920	7.551
Mean nvPM EI_n ($x10^{15}$ kg^{-1})	0.9391	0.9391	1.000	0.9391	0.8926	1.010
Flights forming persistent contrails (%)	54.58	51.68	54.58	54.58	54.68	54.63
Dist. forming persistent contrails (%)	16.21	14.67	16.21	16.21	16.46	16.20
Mean contrail age (h)	3.517	3.205	3.638	3.539	3.550	3.439
Contrail optical depth, τ	0.1215	0.0799	0.1306	0.1240	0.1245	0.1168
Contrail cirrus coverage (%)	0.4730	0.2395	0.5274	0.4775	0.4922	0.4445
Cloud-contrail overlap (%)	75.01	74.75	75.57	75.15	75.21	74.68
SW RF (mW m^{-2})	-236.2	-126.3	-273.7	-239.2	-249.0	-218.0
LW RF (mW m^{-2})	471.4	247.2	540.7	476.3	496.1	436.3
Net RF (mW m^{-2})	235.2	120.8	267.1	237.1	247.1	218.4
Net ERF (mW m^{-2})	98.77	50.75	112.2	99.56	103.8	91.72
$EF_{contrail}$ ($x10^{18}$ J)	62.72	32.47	71.47	63.22	65.98	58.12
$EF_{contrail}$ per flight distance ($x10^8$ J m^{-1})	0.5299	0.2744	0.6039	0.5342	0.5575	0.4911
$EF_{contrail}$ per contrail length ($x10^8$ J m^{-1})	3.269	1.870	3.725	3.295	3.387	3.031
% flights responsible for 80% $EF_{contrail}$	11.97	9.61	11.91	12.05	12.00	11.89

References

Abrahamson, J. P., Zelina, J., Andac, M. G., and Vander Wal, R. L.: Predictive Model Development for Aviation Black Carbon Mass Emissions from Alternative and Conventional Fuels at Ground and Cruise, Environ. Sci. Technol., 50, 12048–12055, https://doi.org/10.1021/acs.est.6b03749, 2016.

Agarwal, A., Speth, R. L., Fritz, T. M., Jacob, S. D., Rindlisbacher, T., Iovinelli, R., Owen, B., Miake-Lye, R. C., Sabnis, J. S., and Barrett, S. R. H.: SCOPE11 Method for Estimating Aircraft Black Carbon Mass and Particle Number Emissions, Environ. Sci. Technol., 53, 1364–1373, https://doi.org/10.1021/acs.est.8b04060, 2019.

Agarwal, A., Meijer, V. R., Eastham, S. D., Speth, R. L., and Barrett, S. R. H.: Reanalysis-driven simulations may overestimate persistent contrail formation by 100-250%, Environ. Res. Lett., 17, https://doi.org/10.1088/1748-9326/AC38D9, 2022.

Boies, A. M., Stettler, M. E. J., Swanson, J. J., Johnson, T. J., Olfert, J. S., Johnson, M., Eggersdorfer, M. L., Rindlisbacher, T., Wang, J., and Thomson, K.: Particle emission characteristics of a gas turbine with a double annular combustor, Aerosol Sci. Technol., 49, 842–855, https://doi.org/10.1080/02786826.2015.1078452, 2015.

Boulanger, D., Bundke, U., Gallagher, M., Gerbig, C., Hermann, M., Nédélec, P., Rohs, S., Sauvage, B., Ziereis, H., Thouret, V., and Petzold, A.: IAGOS Time series [Data set], https://doi.org/https://doi.org/10.25326/06, 2022.

North Atlantic Skies - The gateway to Europe: https://nats.aero/blog/2014/06/north-atlantic-skies-gateway-europe/, last access: 15 October 2021.

Cumpsty, N. A. and Heyes, A.: Jet propulsion: A simple guide to the aerodynamics and thermodynamic design and performance of jet engines, Third Edition., Cambridge University Press, 2015.

Döpelheuer, A. and Lecht, M.: Influence of engine performance on emission characteristics, in: Symposium of the applied vehicle Technology Pane-Gas Turbine Engine Combustion, Emissions and alternative fuels, Lisbon, Portugal, 1998.

DuBois, D. and Paynter, G.: Fuel Flow Method2" for Estimating Aircraft Emissions, J. Aerosp., 115, 1–14, 2006.

Durdina, L., Brem, B. T., Setyan, A., Siegerist, F., Rindlisbacher, T., and Wang, J.: Assessment of Particle Pollution from Jetliners: from Smoke Visibility to Nanoparticle Counting, Environ. Sci. Technol., 51, 3534–

3541, https://doi.org/10.1021/acs.est.6b05801, 2017.

EASA: Implementation of the latest CAEP amendments to ICAO Annex 16 Volumes I, II and III, 2020.

ICAO: Aircraft Engine Emissions Databank (07/2021): https://www.easa.europa.eu/domains/environment/icao-aircraft-engine-emissions-databank, 2021. Last access: 17 August 2021.

Eurocontrol: User Manual for the Base of Aircraft Data (BADA) Revision 3.12., Eurocontrol Experimental Centre, 2014.

Eurocontrol: User Manual for the Base of Aircraft Data (BADA) Family 4, 2016.

Gierens, K., Matthes, S., and Rohs, S.: How Well Can Persistent Contrails Be Predicted?, Aerosp. , 7, 169, https://doi.org/10.3390/AEROSPACE7120169, 2020.

Hersbach, H., Bell, B., Berrisford, P., Hirahara, S., Horányi, A., Muñoz-Sabater, J., Nicolas, J., Peubey, C., Radu, R., Schepers, D., Simmons, A., Soci, C., Abdalla, S., Abellan, X., Balsamo, G., Bechtold, P., Biavati, G., Bidlot, J., Bonavita, M., De Chiara, G., Dahlgren, P., Dee, D., Diamantakis, M., Dragani, R., Flemming, J., Forbes, R., Fuentes, M., Geer, A., Haimberger, L., Healy, S., Hogan, R. J., Hólm, E., Janisková, M., Keeley, S., Laloyaux, P., Lopez, P., Lupu, C., Radnoti, G., de Rosnay, P., Rozum, I., Vamborg, F., Villaume, S., and Thépaut, J. N.: The ERA5 global reanalysis, Q. J. R. Meteorol. Soc., https://doi.org/10.1002/qj.3803, 2020.

Koop, T., Luo, B., Tsias, A., and Peter, T.: Water activity as the determinant for homogeneous ice nucleation in aqueous solutions, Nature, 406, 611–614, https://doi.org/10.1038/35020537, 2000.

Moore, R. H., Thornhill, K. L., Weinzierl, B., Sauer, D., D'Ascoli, E., Kim, J., Lichtenstern, M., Scheibe, M., Beaton, B., and Beyersdorf, A. J.: Biofuel blending reduces particle emissions from aircraft engines at cruise conditions, Nature, 543, 411–415, https://doi.org/10.1038/nature21420, 2017.

Parr, W. C. and Schucany, W. R.: Minimum distance and robust estimation, J. Am. Stat. Assoc., 75, 616–624, https://doi.org/10.1080/01621459.1980.10477522, 1980.

Petzold, A., Neis, P., Rütimann, M., Rohs, S., Berkes, F., G. J. Smit, H., Krämer, M., Spelten, N., Spichtinger, P., Nédélec, P., and Wahner, A.: Ice-supersaturated air masses in the northern mid-latitudes from regular in situ observations by passenger aircraft: Vertical distribution, seasonality and tropospheric fingerprint, Atmos. Chem. Phys., 20, 8157–8179, https://doi.org/10.5194/ACP-20-8157-2020, 2020.

Rädel, G. and Shine, K. P.: Validating ECMWF forecasts for the occurrence of ice supersaturation using visual observations of persistent contrails and radiosonde measurements over England, Q. J. R. Meteorol. Soc., 136, 1723–1732, https://doi.org/10.1002/qj.670, 2010.

Reutter, P., Neis, P., Rohs, S., and Sauvage, B.: Ice supersaturated regions: Properties and validation of ERA-Interim reanalysis with IAGOS in situ water vapour measurements, Atmos. Chem. Phys., 20, 787–804, https://doi.org/10.5194/ACP-20-787-2020, 2020.

Schumann, U.: A contrail cirrus prediction model, Geosci. Model Dev., 5, 543–580, https://doi.org/10.5194/gmd-5-543-2012, 2012.

Schumann, U. and Graf, K.: Aviation-induced cirrus and radiation changes at diurnal timescales, J. Geophys. Res. Atmos., 118, 2404–2421, https://doi.org/10.1002/jgrd.50184, 2013.

Schumann, U., Penner, J. E., Chen, Y., Zhou, C., and Graf, K.: Dehydration effects from contrails in a coupled contrail–climate model, Atmos. Chem. Phys., 15, 11179–11199, https://doi.org/10.5194/acp-15-11179-2015, 2015.

Schumann, U., Poll, I., Teoh, R., Koelle, R., Spinielli, E., Molloy, J., Koudis, G. S., Baumann, R., Bugliaro, L., Stettler, M., and Voigt, C.: Air traffic and contrail changes over Europe during COVID-19: A model study, Atmos. Chem. Phys., 21, 7429–7450, https://doi.org/10.5194/ACP-21-7429-2021, 2021.

Sonntag, D.: Advancements in the field of hygrometry, Meteorol. Zeitschrift, 3, 51–66, https://doi.org/10.1127/metz/3/1994/51, 1994.

Stettler, M. E. J.: Aviation emissions of black carbon and other air pollutants, PhD Thesis, University of Cambridge, 2013.

Stettler, M. E. J., Boies, A., Petzold, A., and Barrett, S. R. H.: Global civil aviation black carbon emissions, Environ. Sci. Technol., 47, 10397–10404, https://doi.org/10.1021/es401356v, 2013.

Teoh, R., Stettler, M. E. J., Majumdar, A., Schumann, U., Graves, B., and Boies, A.: A methodology to relate black carbon particle number and mass emissions, J. Aerosol Sci., 132, 44–59, https://doi.org/10.1016/J.JAEROSCI.2019.03.006, 2019.

Teoh, R., Schumann, U., and Stettler, M. E. J.: Beyond Contrail Avoidance: Efficacy of Flight Altitude Changes to Minimise Contrail Climate Forcing, 7, 121, https://doi.org/10.3390/aerospace7090121, 2020a.

Teoh, R., Schumann, U., Majumdar, A., and Stettler, M. E. J.: Mitigating the Climate Forcing of Aircraft Contrails by Small-Scale Diversions and Technology Adoption, Environ. Sci. Technol., 54, 2941–2950, https://doi.org/10.1021/acs.est.9b05608, 2020b.

Tompkins, A. M., Gierens, K., and Rädel, G.: Ice supersaturation in the ECMWF integrated forecast system, Q. J. R. Meteorol. Soc., 133, 53–63, https://doi.org/10.1002/qj.14, 2007.

Voigt, C., Kleine, J., Sauer, D., Moore, R. H., Bräuer, T., Le Clercq, P., Kaufmann, S., Scheibe, M., Jurkat-Witschas, T., Aigner, M., Bauder, U., Boose, Y., Borrmann, S., Crosbie, E., Diskin, G. S., DiGangi, J., Hahn, V., Heckl, C., Huber, F., Nowak, J. B., Rapp, M., Rauch, B., Robinson, C., Schripp, T., Shook, M., Winstead, E., Ziemba, L., Schlager, H., and Anderson, B. E.: Cleaner burning aviation fuels can reduce contrail cloudiness, Commun. Earth Environ. 2021 21, 2, 1–10, https://doi.org/10.1038/s43247-021-00174-y, 2021.